4 EXPERIMENTAL EQUIPMENT FOR THE 12 GeV UPGRADE

4.A Overview

In this chapter we outline the upgrades and additions to the equipment in the present experimental halls, and the equipment needed for the new hall (Hall D) that is being added to support the meson spectroscopy initiative. The equipment makes efficient use of much of the base equipment from the original CEBAF complement. Both high-resolution spectrometers are retained in Hall A, all of the CLAS components (with the exception of the drift chambers) are retained in Hall B, and the High-Momentum Spectrometer (HMS) is retained in Hall C. These devices are complemented by the addition of a medium-acceptance spectrometer in Hall A (to be called MAD, Medium-Acceptance Device), an upgrade of the central region and tracking system for CLAS in Hall B, a new high-momentum spectrometer in Hall C (the SHMS, Super-High-Momentum Spectrometer), and the new Hall D equipment. These items, and related ancillary equipment, are described in detail in the sections below.

4.B Hall A

4.B.1 Overview

The present base instrumentation in Hall A has been used with great success for experiments that require high luminosity and high resolution in momentum and/or angle for at least one of the reaction products. The central elements are the two High-Resolution Spectrometers (HRS). Both of these devices provide a momentum resolution of better than 2×10^{-4} and an angular resolution of better than 1 mrad. The design maximum central momentum, 4 GeV/c, is available in one of the HRS, but in the other the central momentum is administratively limited to 3.2 GeV/c to avoid possible damage from a short in the copper component of one of the superconducting coils.

The Jefferson Lab 12 GeV (11 GeV for Halls A, B, and C) Upgrade opens several new physics windows. In particular, a large kinematic domain becomes available for studies of deep inelastic scattering. The combination of high luminosity and high polarization of beam and targets will place Jefferson Lab in a unique position to make significant contributions to the understanding of nucleon and nuclear structure and of the strong interaction in the high-x region.

Theoretically, the high-x region provides a relatively clean testing ground for our understanding of nucleon structure in terms of valence quarks, which will dominate this region. Precision data are scarce in this region (especially for the spin-dependent nucleon structure), due to the fact that the quark distribution functions drop rapidly when x becomes large. Such data at relatively low Q^2 are not only important for understanding this structure, but would also have a significant impact on a search for new physics beyond the standard model at very high energies. To fully utilize the high luminosity available at CEBAF, a well-matched spectrometer with large momentum and angular acceptance and moderate momentum resolution is crucial for obtaining precision information in the high-x region.

Table 18 lists the physics requirements of a number of experiments that need a large-acceptance spectrometer, mainly in the high-x region. A brief explanation of these experiments is given in the following paragraphs. Several are discussed in more detail in Chapters 1 and 2. The first experiment uses unpolarized inclusive electron scattering on ^{3}H and ^{3}He [Pe00]. Precision measurements of the d-quark-to-u-quark ratio at high x, through the study of the ratio of the ^{3}H and ^{3}He structure functions, will resolve a long-standing issue of different predictions from pQCD and constituent quark models. This experiment also requires the implementation of a ^{3}H target. The second will provide a precise measurement of the spin structure functions g_1 and A_1 of the neutron by using a polarized ^{3}He target [Me00]. It will unambiguously establish the trend of A_1^n for $x \to 1$, which will

Table 18: Instrumentation requirements for experiments needing a large-acceptance detector.

Nr.	Exp.	P_{max} (GeV/c)	Angle acc. (msr)	Mom. acc. (%)	Mom. res. (%)	Hor. ang. res. (mrad)	Vert. ang. res. (mrad)	Min. angle (degrees)
1	^{3}H/^{3}He	6	15-30	30	0.3	1	3	15-30
2	A_1^n, g_1^n	5-7	15-30	30	0.3	2	3	15-30
3	g_2^n	5	20-30	30	0.3	2	3	15-25
4	A_1^p, g_1^p	5-7	15-30	30	0.3	2	3	15-30
5	DIS-PV	6	30	30	0.3	1	3	15-25
6	Semi-π	6-7	10-30	30	0.3	2	3	12-15
7	Semi-K	6-7	10-30	30	0.3	2	3	12-15
8	Charm	6.5	30	30	0.3	1	2	12-15
9	b_1	6	15-30	30	0.3	1	3	20-30
10	Recoil p	5-7	10-30	30	0.3	1	3	15-25

provide a benchmark test of pQCD and constituent quark models. Precision measurements of g_1 will also provide vital information on nucleon spin structure.

The third experiment [Av00] will measure the g_2^n spin structure function and its moments. This measurement will be a clean measure of a higher twist effect (twist 3), which is related to the quark-gluon interaction. The fourth is the equivalent of the second for the proton [Mi00]. Parity violation in deep inelastic scattering (the fifth experiment) can be used to selectively study nucleon structure, quark-quark correlations, or the standard model [So00].

With high luminosity and well-matched spectrometers, a new window opens in the study of nucleon structure and the strong interaction: semi-inclusive reactions can be used to probe the structure of the parton distributions. Experiments six and seven are examples of a potentially very rich program using semi-inclusive reactions to test factorization and to study the flavor decomposition of the nucleon spin structure, the asymmetry of the sea quark distribution, and the Generalized Parton Distributions [Gi00].

With an 11 GeV beam, the threshold of charm production is crossed. Threshold charm production (experiment 8, [Chpc]) allows one to study the role of the gluons in nucleon structure and some other novel phenomena, such as hidden color. A measurement of the charm-nuclear cross sections will also provide important information for RHIC physics.

The measurement of b_1 (experiment 9, [Mi00]) studies the spin 1 system with a tensor-polarized

Table 19: Summary of major design specifications for the large-acceptance spectrometer

Angular acceptance	30 msr (at a scattering angle of 30°) to 15 msr (at 15°)
Momentum acceptance	30%
Maximum central momentum	5–7 GeV/c
Minimum scattering angle	12–25° (reduced solid angle at small angles)
Moderate resolutions	0.3% in momentum, 1 (3) mrad in hor. (vert.) angle.

deuteron target. This provides a unique channel for a study of the difference between the deuteron system and a trivial bound state of two spin 1/2 objects coupled to spin 1. Many other experiments, such as real and deeply virtual Compton scattering (experiment 11, [Wopc]), will also benefit from a large-acceptance, moderate-resolution spectrometer. Compton scattering experiments also require a high-performance electromagnetic calorimeter.

Three major instrumentation upgrades are proposed to allow an optimal study of the experiments listed in the previous section: a large-acceptance spectrometer, a high-resolution electromagnetic calorimeter, and a ^{3}H target. The spectrometer would provide a tool for high-x studies of the properties of nucleons with an 11 GeV beam, where a large acceptance in both solid angle and momentum coupled to a moderate momentum resolution is needed.

The availability of a high-intensity 11 GeV beam will offer unique possibilities for studying both real and virtual Compton scattering. These experiments require the construction of a large, highly segmented, electromagnetic calorimeter. Other experiments besides Compton scattering will no doubt also benefit from such a detector. The proposed measurement of the d-quark-to-u-quark ratio requires a tritium target.

4.B.2 A New, Medium-Acceptance Device (MAD)

General characteristics

The proposed MAD (Medium-Acceptance Device) detector is a magnetic spectrometer built from two combined-function, quadrupole and dipole, superconducting magnets with a maximum central momentum of 6 GeV/c and a total bend angle of 20°. Extra versatility can be achieved by varying the drift distance to the first magnet. Larger drift distances allow smaller scattering angles at the cost of reduced acceptance.

Table 20: Performance parameters of the MAD spectrometer

Minimum angle 35°		Minimum angle 25°	
Acceptance	Resolution	Acceptance	Resolution
$\theta_0 \pm 207$ mrad	$\sigma_\theta = 3.5$ mrad	$\theta_0 \pm 165$ mrad	$\sigma_\theta = 3.0$ mrad
$\phi_0 \pm 38$ mrad	$\sigma_\phi = 0.8$ mrad	$\phi_0 \pm 35$ mrad	$\sigma_\phi = 1.0$ mrad
$y_0 > \pm 5$ cm	$\sigma_y = 2.5$ mm	$y_0 > \pm 5$ cm	$\sigma_y = 4.0$ mm
$\delta \pm 15\%$	$\sigma_\delta = 0.26\%$ @ $\delta = 15\%$	$\delta \pm 15\%$	$\sigma_\delta = 0.26\%$ @ $\delta = 15\%$

Depending on the details of the detector package, scattering angles as small as 12° might be possible. The quadrupole components provide the focusing necessary to achieve the desired solid angle while the dipole components provide the dispersion needed for momentum resolution. Optical properties and their impact on the performance have been studied. A description of those studies and their results follows. Table 20 shows the estimated performance parameters based on TRANSPORT [Br80a] calculations of the optical properties.

Optical design

A working model of the MAD spectrometer has been developed using the raytracing code SNAKE [Ve87]. The magnetic fields in the magnets are determined using TOSCA [TOSCA]-generated maps. The first was generated by running TOSCA on the magnet with only the quadrupole coil energized and the second with only the dipole element energized. These two maps are then added together with scale factors to simulate tuning the relative excitation of the quadrupole and dipole components of each of the magnets, until the first-order properties expected from the TRANSPORT studies are reproduced. Then, a large number (2000) of random trajectories spanning the full acceptance of the spectrometer are traced through the spectrometer. These trajectories are then used as input to a fitting program that determines the best-fit polynomials which reproduce the target parameters $(\delta, \theta_0, y_0, \phi_0)$ of the input trajectories based on their positions and angles $(x_f, y_f, \theta_f, \phi_f)$ in the detectors. The sensitivity to measurement errors in the detectors can then be explored in a Monte Carlo fashion using a new set of trajectories generated in the same manner as those used in the fitting. In general there is a reasonable match between the Monte Carlo analysis and the TRANSPORT-based predictions.

A set of simulations has been performed to evaluate the performance of the MAD spectrometer using the existing polarized ^{3}He target in the 25° configuration. The spectrometer was equipped with an H_2 bag in the body of the spectrometer followed by two wire chambers separated by just

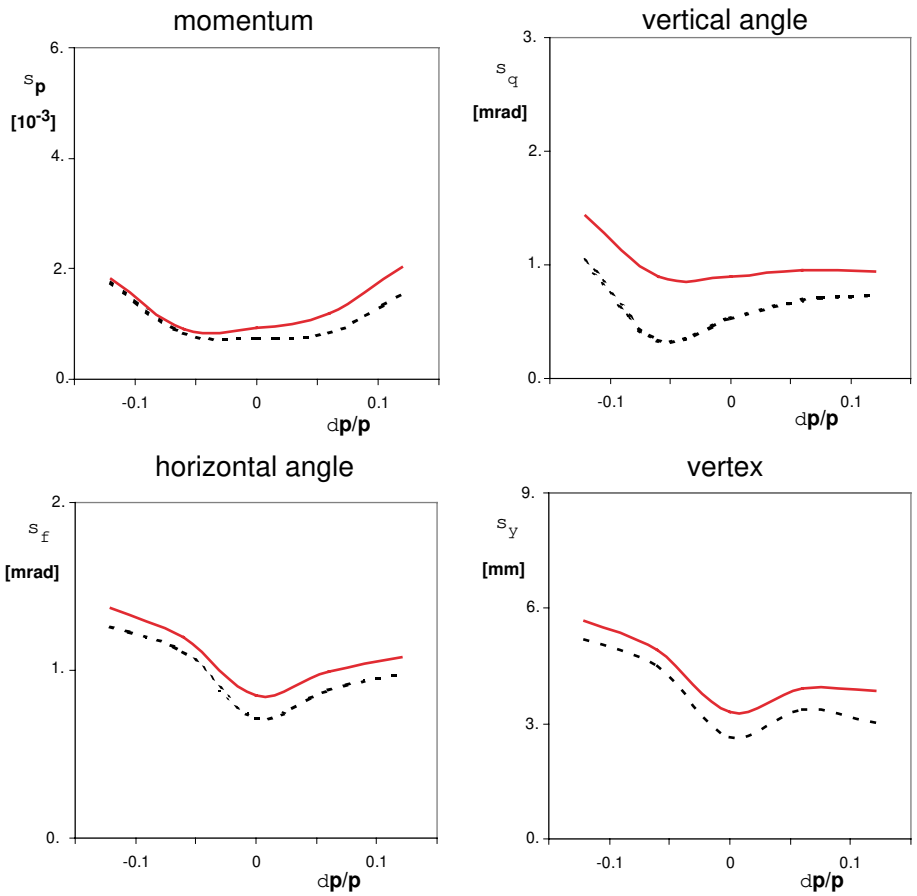

Figure 71: Resolution in δ, θ_0, y_0, and ϕ_0 as a function of the particle momentum. Dashed line: optical resolution, assuming a 200-μm-diameter beam spot. Solid line: result of the full Monte Carlo simulation, including multiple scattering.

over 1 m. Trajectories spanning the full momentum acceptance were evaluated in five momentum bins centered at δ = -12, -6, 0, 6, and 12%. The effect of multiple scattering in the target on the initial trajectories and of multiple scattering in the H_2 bag, the exit window, the first wire chamber, and the air between the wire chambers on the determination of the final trajectories $(x_f, y_f, \theta_f, \phi_f)$ was evaluated. Then the effect of those uncertainties on the original trajectory parameters (δ, θ_0, y_0, and ϕ_0) was evaluated, assuming a 200 μm beam spot, in a Monte Carlo fashion using $\sim$ 400 random trajectories spanning the full acceptance of the spectrometer in each momentum bin. The effects from the target and the rest of the spectrometer on δ, θ_0, y_0, and ϕ_0 were then added in quadrature. Multiple scattering was evaluated separately for the central momentum of each bin.

Figure 71 shows the resolution of δ, θ_0, y_0, and ϕ_0 generated in the Monte Carlo analysis for

two cases: (1) No measurement error. This demonstrates how well the optics are understood and incorporates the effect of a 200 μm beam spot. (2) Full MC results taking into account multiple scattering in the target, various windows, and detector components.

The large fields and field gradients in the magnets in the 6 GeV/c version of the MAD preclude the possibility of achieving a higher central momentum by simply increasing the fields in the magnets. Therefore, to reach a higher central momentum the magnets must be lengthened. For example, increasing the maximum central momentum to 8 GeV/c results in a loss of angular acceptance of $\approx 25\%$ unless the apertures are increased proportionately. However, the large fields and field gradients needed in the magnets also preclude an increase in the apertures. A decrease in the bend angles of both magnets will also accommodate an increase in the maximum central momentum at an expected moderate loss of resolution. However, this would increase the acceptance region with a direct line-of-sight between target and detector, the effect of which requires further study.

Magnet design

This spectrometer requires a pair of identical combined-function superconducting magnets that can simultaneously produce a 1.5 T dipole field and a 4.5 T/m quadrupole field inside a warm bore of 120 cm (QD120SC). A magnetic design using TOSCA3D has been performed to establish the basic magnetic requirements, provide 3D field maps for optics analysis, and produce basic engineering information about the magnets. A two-sector $\cos(\phi)/\cos(2\phi)$ design with a low nominal current density (5750/4111 A/cm^2) with a warm bore and warm iron has been selected and analyzed. These low current densities are consistent with the limits for a cryo-stable winding. Coils of this type are generally the most conservative that can be built, and the large size and modest field quality requirements (3×10^{-3}) ensure that construction tolerances (1–2 mm) are easily achievable. Other relevant parameters of the QD120SC magnet are given in Table 21.

The magnetic design uses TOSCA-generated $\cos(\phi)$ type coils with "constant perimeter ends". These coils closely approximate the ideal cosine geometry that is well established as a "perfect" generator of high-purity fields. Practical considerations (finite current distributions, limited number of sectors, and TOSCAs internal approximations) contribute to deviations from the ideal geometry and are the sources of higher-order field errors in the design. The yoke is modeled as truly nonlinear iron with the nominal properties of 1010 steel. The present yoke design is a simple 3.0-m-long annulus with a 3.2 m OD and a 2.0 m ID. The yoke variations that have been studied are a full-coverage 4.0 m cylinder, beveled ends, a truncated 3.0 m cylinder, and a beam tube slot. Due

Table 21: Magnet properties

Type	Combined-Function QD
Aperture	120 cm warm bore
NI:	
dipole	2.3×10^6 A turns
quad	4.9×10^6 A turns
Central field	1.5 T
Dipole $\int Bdl$	3.6 Tm
Quadrupole $\int Gdl$	13.0 (T/m)m (gradient $G = 4.2$ T/m)
Effective length:	
Dipole	2.4 m
Quad	3.1 m
Overall length	4 m (3.2 m central length with 0.4 m step ends)
Yoke	130 metric tons warm iron (1010 steel) (3.2 m OD $\times$ 2.0 m ID $\times$ 3.0 m long)
Coil and cryostat:	25 metric tons stainless steel (2.0 m OD $\times$ 1.2 m ID $\times$ 4.0 m long)
Peak linear force density:	
dipole coil	36,000 lbs/in (peak pressure 1100 psi)
quad coil	39,000 lbs/in (peak pressure 1300 psi)
Total peak pressure:	2400 psi
Stored energy:	15 MJ

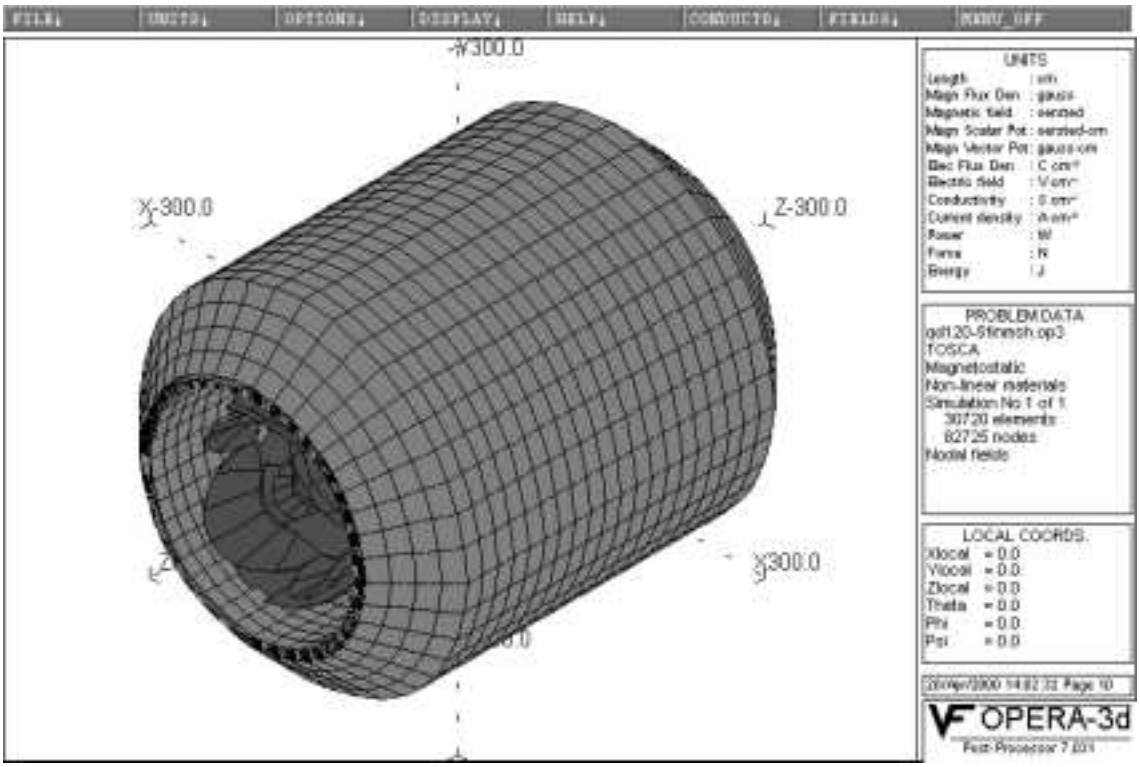

Figure 72: TOSCA 3D grid of the iron yoke with the coil package inside.

to the nature of current-dominated coils and largely unsaturated iron, these variations have little effect on the internal fields, allowing a maximum freedom of choice in the final design. The present results of the optics analysis based on this magnetic design indicate that the field quality achieved is already at a level that meets the requirements, so no further "trimming" is anticipated. Relevant results of the TOSCA calculations are shown in Figs. 72 and 73.

The QD120SC combined-function magnet produces peak fields in the warm bore of 4 T and peak fields in the windings of 5 T. These fields are comparable to those achieved in large-bore magnets produced 20 years ago for MHD (Magneto-Hydro-Dynamics) research, particle spectroscopy, and coal sulphur separation (see Table 22). There are significant differences as well between the present magnet and these "prototypes". For example, the stored energy of the QD120SC is typically less even though the field volumes are comparable. This is due to the fact that the superposed quadrupole field produces significantly less stored energy for a given maximum field. The combined fields also produce a very asymmetric field and force distribution. The fields add on the bottom of the magnet and subtract on the top, resulting in fields across the bore ranging from -1 to 4 T.

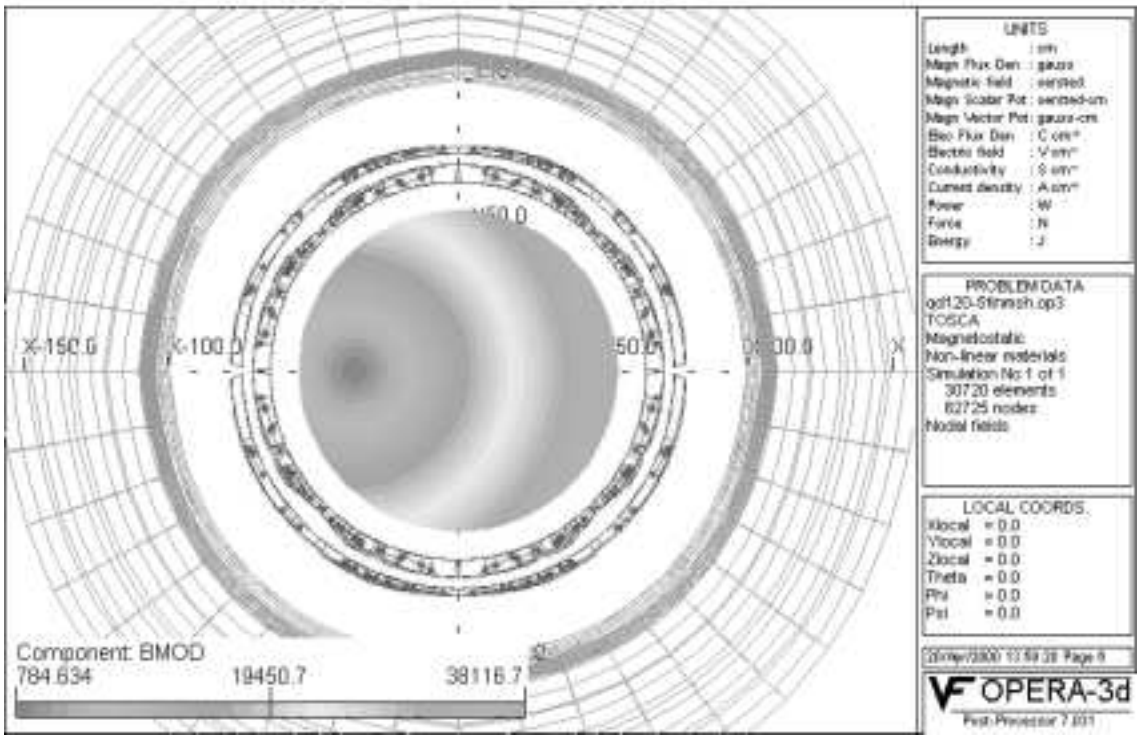

Figure 73: TOSCA-generated modulus of the magnetic field in the aperture, showing a quadrupole field configuration offset to the left of the magnet center.

Table 22: Large-aperture superconducting magnets

Magnet	Reference
U25 SC Dipole Magnet for MHD	[Ne77]
UTSI SC Dipole Magnet for MHD	[Wa82]
CFFF SC Dipole Magnet for MHD	[Wa80]
Omega Spectrometer SC Dipole	[Mo70]
Large SC Dipole Spectrometer Magnet	[Mo79a]
Large SC Dipole for Spectrometer	[Wo81]
Super Benkei SC dipole magnet for spectrometer	[In84]

Hence, there is a net force between the yoke and coil. The peak linear forces add on one side and subtract on the other, yielding peak pressures that range from 2400 psi to 300 psi. Due to the large radial thickness (12 cm) of the windings and cryostat (40 cm), the required 11-cm-thick pressure shell is easily accommodated without stressing the coil cold mass. The large size of the cryostat will allow separate fluid pressure vessels in accordance with the ASME code. A fully clamped winding is planned for the final construction. This combined with the very conservative cryo-stability will result in a highly reliable design.

The cryogenics for the combined-function magnets will be based on the very successful thermal-siphon cooling that has been incorporated in nearly all the superconducting magnets at JLab. The very high (100 g/s) internal flow rates and simple reservoir level control ensure very reliable operation with simple controls. The heart of this system is a somewhat complex control reservoir that contains JT valves, bayonet connections, phase-separating reservoirs, current leads, relief valves, and instrumentation including level sensors. There are four of these control reservoirs at JLab and three more being delivered. The standardization of design and function of components will ensure compatibility and reliability. The control reservoir will be mounted on the downstream ends of the magnets and will be located on the side to keep the overall spectrometer profile low enough to fit through the truck access door of Hall A. The cryogenic valving allows for top and bottom fill of helium and nitrogen for level operation and cooldown. There will also be a separate valve for variable-temperature cooldown gas made locally in an LN2 to He gas heat exchanger (also standard design). This will be used to cool down and warm up the magnets to minimize thermal stress due to relative contraction and to increase the overall efficiency of cryogenic operations.

Helium at 3.0 atm and 4.5 K is supplied from the End Station Refrigerator (ESR) and JT expanded in the magnet to fill the reservoir. The on-board phase separator allows efficient return of

cold gas to the ESR while filling the reservoir without disturbing the level indication. Cold return and warm return shutoff valves are included to allow a smooth transition from cooldown to regular closed-cycle operation. Similarly, LN2 is supplied at 80 K and 2 to 4 atm. Gaseous N2 is vented at the magnet to a sealed exhaust line. Separate flow control and measurement for each current lead is a normal part of this design. Finally, the reservoirs contain dual relief devices, an ASME coded mechanical relief, and a rupture disc set at a 25% higher pressure. Exhaust lines for pressure relief, separate from cooldown lines, are used so that there is no chance of a contamination blockage in these important pressure relief paths. The reservoirs contain temperature sensors, liquid level sensors and voltage taps. Generally, all internal instrumentation is routed to the reservoir through a set of vacuum feedthroughs. Strain gauges in the cold-to-warm support system will be essential due to the force between yoke and coil especially considering the asymmetry of these forces. Vacuum gauging and system pressure sensors will also be located in the control reservoir. JLab owns the design for the installed and to-be-delivered control reservoirs, all of which were built commercially; thus a repeat order could be easily accomplished.

Tuning of the MAD spectrometer requires both relative polarities, so the magnets must be identical and the quadrupole/dipole components must be independently operable. DC power for the magnets is presently designed around low-voltage, high-current commercial power supplies. A DC current of 5 kA at 10 V would be a safe choice due to the relatively low inductance (1.2 H) and provide easily for a charge time under 30 minutes. JLab has three power supplies obtained from SSC surplus that could easily be used. Fast discharge voltages under 500 V are easily obtained with a high-current design, thus reducing the risk of exposure to high voltages. The very large cold mass and low current density ensure that sufficient material is available in the cold mass to absorb most of the stored energy at a low temperature during a quench discharge.

A conceptual design for the MAD support structure has been completed, the result of which is shown in Fig. 74. The support structure was required to allow positioning the MAD spectrometer through a range of angles including the lower-acceptance 15° to 30° range and the 35 msr acceptance 30° through 90° range. This is accomplished by the use of a sliding suspension that permits the magnets and detector to be moved closer to or further away from the pivot.

The construction of the support structure must allow assembly inside Hall A. The structure is comprised of about 20 pieces each under the 20 ton crane capacity. The magnets and detector are carried on transport carts to permit angle changes. They can also be withdrawn up the truck ramp one at a time so that the major MAD components can be "parked" at large angles out of the way of the normal HRS operating range. This is accomplished by steerable Hillman rollers on each transporter and a track in the truck entrance. The magnets are "driven" onto the support

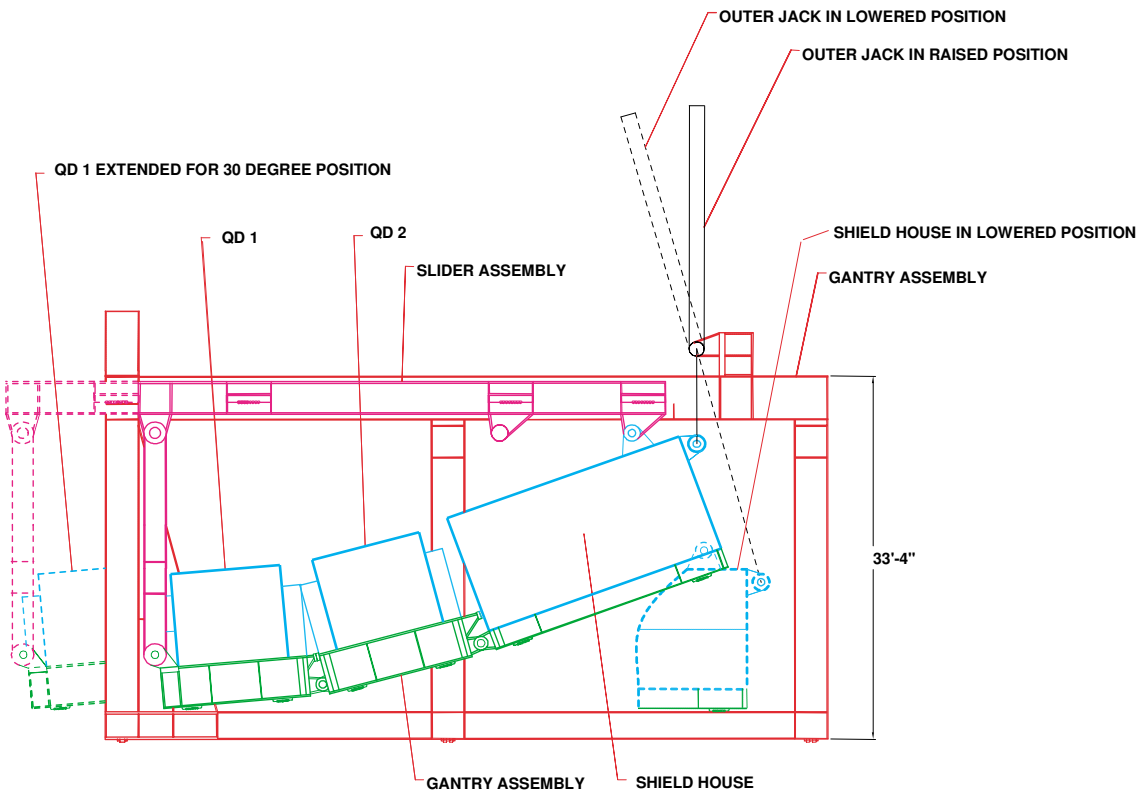

Figure 74: Side view of the support structure for MAD.

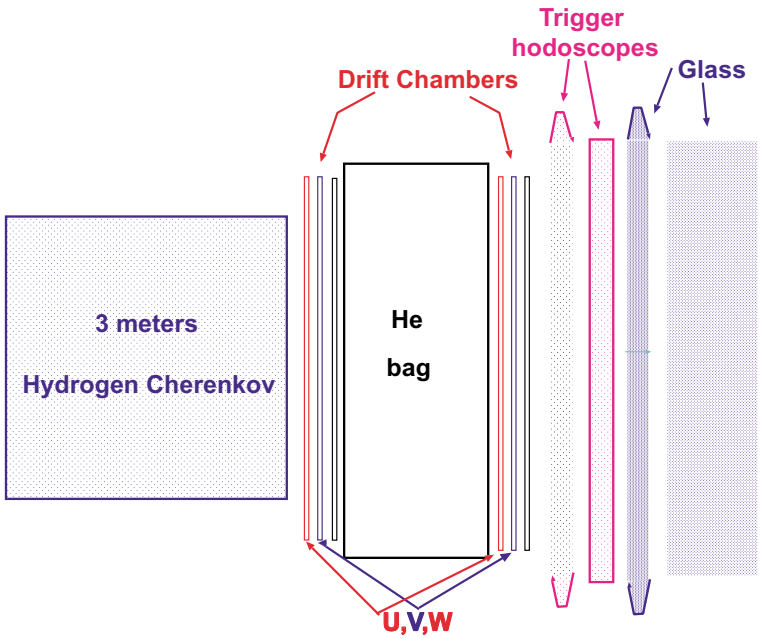

Figure 75: Schematic layout of the basic detector system planned for the proposed MAD spectrometer.

structure and linked together to put them into use. The linked components can then be lifted to their proper attitude with a hydraulic system, which uses components similar to those in the Hall C SOS system. Remote operation of angle changes is not anticipated at this time. The conceptual design as presented meets all operating requirements and assembly and disassembly conditions.

The detector system

The proposed basic detector package for the MAD spectrometer will serve for most electron scattering experiments. The detectors have been designed to cover the full momentum and angular acceptance. The design includes an optional hadron configuration with a flexible particle identification system in the trigger and a very powerful PID in the off-line analysis.

The main components of the detector package are as follows (with rms values of perfomance parameters for 6 GeV electrons listed):

- High-resolution drift chamber – 75 μm per plane and 0.30 mrad angular.
- Hydrogen gas Čerenkov counter – 2 m long, ten photoelectrons, $P^{\pi}_{\rm threshold} \sim 8$ GeV/c.

- Trigger scintillator counters – 70 ps, two layers, each 5 cm thick, of BC408 scintillating material.
- Lead glass hadron rejector – a hadron suppression factor of a few $\times 100$.

The main components of the hadron configuration are:

- Variable-pressure gas Čerenkov counter – 100 cm long, $\gamma_{\rm threshold}$ range of 8 to 32.
- Diffuse reflective aerogel counter A1, $n = 1.008$ (1.015) – 50 cm long.
- Diffuse reflective aerogel counter A2, $n = 1.030$ (1.060) – 50 cm long.
- Ring imaging Čerenkov counter – 140 cm long.

Triggering and tracking For triggering, two plastic scintillator hodoscopes will be located behind the drift chambers. Each hodoscope will have 16 paddles ($2 \times 5 \times 60$ cm^3) viewed by two XP2282 PMT's. A classical pair of drift chambers 1 m apart with 1 cm drift distance will be used for particle tracking. Each drift chamber contains three groups (4U,4V,4W) with wires oriented differently, each with four wire planes. The four planes in each direction provide high efficiency and resolution. The extra group W enhances high-rate operation. The total number of wires in each chamber is about 1700.

The lead glass shower counter A lead glass preshower/shower combination will provide identification of electrons. The preshower layer consists of 40 modules, each $13 \times 13 \times 35$ cm^3, arranged in four layers. The shower layer consists of 100 similar modules.

The hydrogen gas Čerenkov counter The refractive index (n-1) of hydrogen gas is 1.4×10^{-4} at atmospheric pressure, which corresponds to a threshold gamma factor of 58. The number of Čerenkov photons detected by a PMT from a 3 m pass through hydrogen will be about ten. This value is based on our experimental results with the Hall A gas Čerenkov counters. The advantages of the hydrogen radiator are very low multiple scattering, reduced delta ray production, and low scintillation light yield. In the present design the front window is inside the magnetic field so that delta rays produced in the window are deflected away from the PMT's. With this feature a high rejection factor for hadrons (few $\times 10^4$) can be achieved.

A variable-pressure gas Čerenkov counter The refractive index (n-1) of isobutane is 1.9×10^{-3} at atmospheric pressure which corresponds to a threshold gamma factor of 16. The number of Čerenkov photons detected by a PMT from a 1 m pass through this gas will be about 40. With a pressure range between 0.25 and 2 atm the counter will provide pion discrimination in a momentum range of 1.6–4.5 GeV/c.

The aerogel trigger Čerenkov counter The radiator has ten layers of 100 aerogel modules, each $11 \times 11 \times 1$ cm^3. Twenty 5" XP4582B PMT's are used for light collection.

The ring imaging Čerenkov counter PID over a wide momentum range coupled to a high-selection PID factor $\sim 10^5$ (*e.g.*, for semi-exclusive kaon production) can be provided by a Ring Imaging Čerenkov counter. In the last few years several successful RICH systems were developed at CERN/SLAC/DESY. A CsI photocathode-based detector is under construction for a Hall A HRS by the INFN/SANITA group. An aerogel and a gas radiator, read out by multi-anode phototubes, are being considered for the present proposal.

4.B.3 High-performance electromagnetic calorimetry

A highly segmented total absorption calorimeter is proposed for use in conjunction with the magnetic spectrometers in high-luminosity Compton experiments (real and virtual) at 11 GeV. The calorimeter must combine high spatial resolution, good energy resolution, fast time response, and substantial radiation hardness.

A calorimeter of 1000 PbF_2 crystals, each $2.5 \times 2.5 \times 15$ cm^3 is proposed. Each crystal will be coupled to a mesh PMT, *e.g.* Hamamatsu R5900 for optimum time resolution. The PMT signals will be digitized by a 1 GHz fast-sampling ADC system, for off-line suppression of pile-up.

PbF_2 is an attractive Čerenkov medium for electromagnetic calorimetry. Some basic properties of PbF_2 are listed in Table 23 and compared with the Pb-Glass already in use for the calorimeter for the Real Compton Scattering Experiment E99-114. The table also illustrates $PbWO_4$, which is a scintillator, and can achieve high energy resolution. However, as a scintillator, $PbWO_4$ is much more sensitive to neutrons and other hadronic background. Additional tests are required to evaluate the selection of calorimeter material.

The calorimetry requirements are most stringent for Deeply Virtual Compton Scattering

Table 23: Comparison of Pb-glass, PbF_2, and $PbWO_4$ properties.

	Pb-Glass TF-1	PbF_2	$PbWO_4$	
Radiation length X_0 (cm)	2.5	0.93	0.89	
Moliere radius r_0 (cm)	3.3	2.2	2.2	
Density ρ (g/cm^3)	3.86	7.77	8.28	
Mass/element (g)	2980	990	1010	$\rho \times (1.33r_0)^2 \times 16X_0$
Photoelectrons/GeV	1100	1600	5000	
Critical Energy (MeV)	15	8.6		

(DVCS) in which an energetic photon must be detected in the direction of the $\vec{q}$-vector (angles as small as 10°) and with a luminosity of at least $10^{37}/\text{cm}^2/\text{s}$. It is important to resolve the exclusive DVCS process from competing inelastic processes such as $ep \to e'p'\pi^0 \to e'p'\gamma\gamma$ or $ep \to e'N^*\gamma \to e'N\pi\gamma$. For different calorimetry materials, Fig. 76 illustrates the kinematic limit for separation of the exclusive channel by $p(e,e'\gamma)X$ double coincidences alone. Beyond the limits illustrated in the figure, the exclusive $ep \to ep\gamma$ channel can be resolved by detecting the recoil proton in triple coincidence. In the DVCS limit, the angular resolution required on the detection of the proton is approximately a factor of 10 less stringent than the requirements for the photon. A high-performance calorimeter can greatly enhance the capabilities for real and virtual Compton scattering experiments at 11 GeV.

4.B.4 A ^{3}H Target

Several experiments have been discussed which require a tritium target. Tritium targets have been used in the past 15 years at Bates [Be89], Saclay [Am94], and most recently at Saskatoon. Those designs have been reviewed, and options have been discussed with knowledgeable people from each of the labs. The target is technically straightforward, but some modifications of the hall will be required for safety purposes.

The three types of targets which have been used are sealed-liquid (Saclay) and high-pressure cold gas (225 psi at 45 K) with a uranium getter storage bed (Bates), and medium-pressure warm gas with a uranium storage bed (Saskatoon). The luminosity requirements of the JLab target will require either a liquid or high-pressure cold gas target.

The major considerations in the target design are to minimize the amount of tritium, minimize

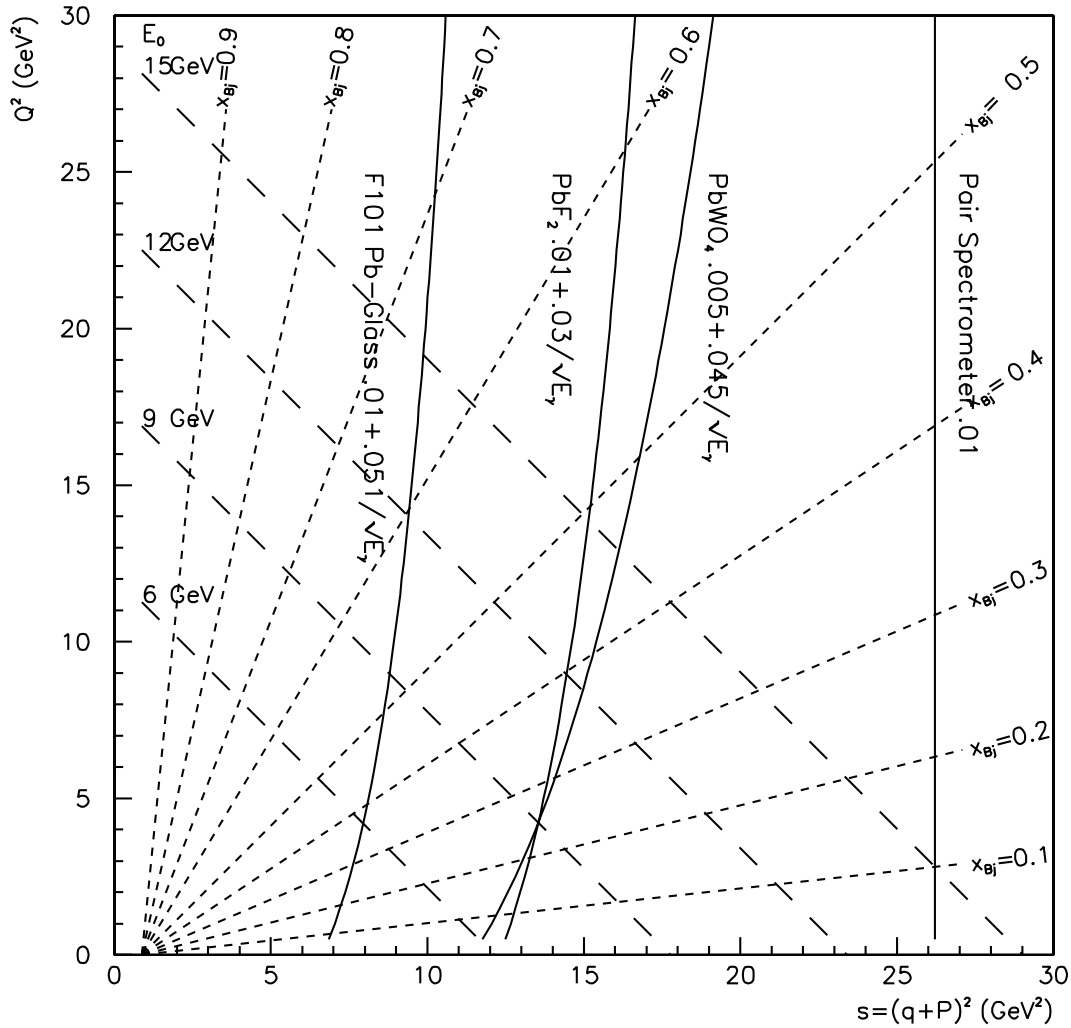

Figure 76: Photon resolution on a plot Q^2 vs. s. The curves labeled by different photon energy resolution values correspond to the kinematic limit at which the $p(e,e'\gamma)p$ and $p(e,e'\gamma)N\pi$(threshold) reactions are separated by 1-σ in the forward (DVCS) limit. DVCS kinematics corresponds to Q^2 and $s=(q+P)^2$ large, and $t=(P'-P)^2 \ll Q^2$. For each resolution curve, the entire kinematic region to the left is accessible with the exclusive channel resolved by $p(e,e'\gamma)X$ double coincidence. Each calorimetry material is labeled with its resolution in $\sigma(E_\gamma)/E_\gamma$. Contours of constant $x_{\rm Bj}$ and constant incident energy E_0 are also indicated separately.

Table 24: Some properties of tritium gas and liquid targets. Activity per cm assumes 1.5-cm-diameter gas target and 1-cm-diameter liquid target. Cooling power listed is due to beam heating only at maximum current. The luminosity is at maximum current. The liquid density is given at 225 psi and 45 K.

State	Density (g/cm^3)	Current (μA)	Cooling (W/cm)	Luminosity (cm^2s^{-1})	Activity/cm (kCi)
Gas	0.028	80	2.9	2.8×10^{36}	0.5
Liquid	0.27	15	5.5	5.1×10^{36}	2.2

the uncertainty in density, match the spectrometer acceptance, and maximize the luminosity. For safety considerations, the maximum amount of tritium should be no more than 20–30 kCi. This limits the maximum target length to around 10 cm for liquid and 40 cm for gas.

Adequate cooling of a liquid target requires most of the target to be surrounded by a copper heat transfer shield, which means only one spectrometer can be used, and the maximum current is about 15 μA. The advantage of liquid is a well-known density (to about 0.5%) and higher luminosity than gas at larger spectrometer angles. The effective density decreases by about 1.5%/μA. The gas target has the advantages that it can be made longer, thus taking advantage of the full acceptance at smaller angles, can take more current, has a more stable density (although presently the density of cold gas is known to only around 1.5–2%), and can be used for coincidence experiments. At large angles the luminosity is about half of that for the liquid one.

The properties of liquid and gas targets are summarized in Table 24. Because of the ability to do coincidence experiments, the better match to the spectrometer solid angle, less stringent cooling requirements, and the more stable density as a function of current, the gas target is preferred. The absolute density can probably be determined by comparing with measurements at higher temperatures and lower pressures where the gas properties are more reliably calculated.

The other question is whether to use a sealed target or storage beds. The advantage of a storage bed is that it provides the possibility to remove the tritium from the target to a mechanically strong container for work on the target or for safety reasons. Storage beds appear to be the best option. The major improvement required for the hall will be a tritium exhaust stack, which would, in the worst case of a complete target rupture, vent the tritium out of the hall with sufficient height and speed to keep the exposure at ground level to an acceptable level (less than 100 mrem at the site boundary).

4.C Hall B

4.C.1 Overview

The Upgrade of CEBAF to 12 GeV will provide opportunities for exciting new physics. The existing CLAS detector in Hall B was designed to study multiparticle, exclusive reactions with its combination of large acceptance and moderate momentum resolution. Studying exclusive reactions at high energy offers a new window on quark subprocesses; the extra information gained from measuring the hadrons' three-momenta allows the controlled study of an additional internal degree of freedom. For example, we can study the perpendicular as well as the parallel component of the quark momentum distributions by analyzing the exclusive production of mesons in the Deep Exclusive Scattering (DES) regime (high Q^2 and W, small t), impossible to deduce from the more limited information content of Deep Inclusive Scattering (DIS). High-energy exclusive events are characterized by higher-momentum, forward-going particles produced in conjunction with the typically lower-energy, larger-angle recoil nucleon system. Moreover, many reactions of interest, such as DES processes, have low cross sections on the order of nb/GeV^2 which will require high-luminosity operation.

To systematically study these high-energy exclusive processes, an upgraded CLAS will retain its toroidal magnet, time-of-flight counters, Čerenkov detectors, and shower counter. The present drift chamber system will be replaced with higher-granularity forward tracking chambers covering the angular range of 5° to 40°. The smaller drift cells result in a smaller sensitive time, making high-rate data collection possible, and also afford better spatial and hence, momentum resolution. The additional electromagnetic background at high luminosity (primarily Møller electrons) will be handled by a solenoidal magnetic shield. A cylindrical drift chamber followed by time-of-flight scintillators and a high-density shower counter will be located within the solenoid, forming the central detector (CD) whose primary role will be detecting the recoil nucleon and other large-angle tracks (35° to 120°). The target location will be moved upstream 1 m to provide coverage down to lab angles as small as 5°. Special (GAP) tracking chambers and shower counters located in front of the main torus coils will enable full azimuthal coverage for photons as well as charged track angular reconstruction down to 5°. These changes will enable efficient reconstruction of exclusive events at luminosities up to 10^{35} cm^{-2} s^{-1}.

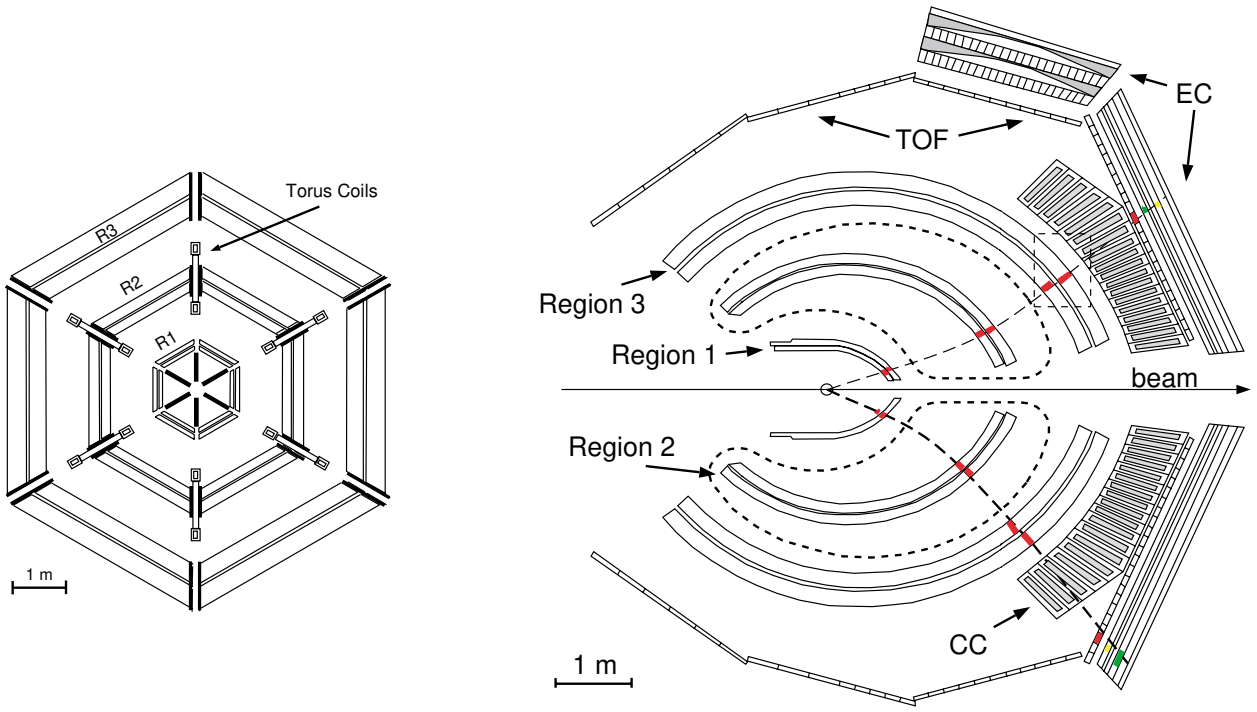

Figure 77: a) View of the CLAS in the beam direction, cut at the target z-position, showing three layers of tracking chambers (left). b) Top view; shown are the three regions of drift chambers, and the CC, EC, and TOF counters (right). A projection of the magnet's cryostat onto the midplane is shown as a dashed line.

4.C.2 Present CLAS Spectrometer

CLAS is a magnetic six-gap spectrometer with a toroidal magnetic field which is generated by six superconducting coils arranged around the beam line to produce a field which is primarily azimuthal; each gap is referred to as a sector. A view of the particle detection system in the direction of the beam (cut in the target region) is given in Fig. 77a, a top view in Fig. 77b. The detection system consists of drift chambers to determine the tracks of charged particles, gas Čerenkov counters for electron identification, scintillation counters for the trigger and for measuring time of flight, and electromagnetic calorimeters to detect showering particles like electrons and photons. The sectors are individually instrumented to form six independent magnetic spectrometers. This facilitates pattern recognition and track reconstruction at high luminosity.

In each sector, charged particles are tracked by drift chambers whose wires are arranged in 3 regions: Region 1 chambers are in the field-free volume close to the target, Region 2 are between the

coils, and Region 3 lie outside of the coils. Each drift chamber region defines an independent track segment. The combination of axial wires oriented perpendicular to the beam axis, and stereo wires oriented at 6° with respect to the axial wires, allows a complete geometric reconstruction of charged tracks. For electron scattering experiments, a small normal-conducting toroid ("mini-torus") surrounding the target and nested within Region 1 keeps (low-momentum) charged electromagnetic background from reaching the Region 1 drift chamber.

The threshold gas Čerenkov counters are sensitive to particles with $\beta \geq 0.998$. In combination with the electromagnetic calorimeters they give good electron identification, sufficient even at large electron scattering angles where the π/e ratio becomes large. The location of the Čerenkov counters in front of the scintillation counters minimizes photon conversion and knock-on electrons.

The scintillation counters serve the dual purpose of contributing to the first-level trigger and providing time-of-flight information. Each counter is viewed by phototubes at both ends for improved timing and position resolution. Both the amplitude and time signals are measured.

The electromagnetic calorimeters are used for the identification of electrons and the detection of photons from the decay of hadrons, such as π^0, η, η', and Λ^*. The calorimeters are made of alternating layers of lead sheets as showering material and plastic scintillator strips. Six forward calorimeter segments provide coverage up to 45° in all six sectors; two additional segments cover the angular range up to 75°.

A Møller polarimeter to measure the polarization of the incident electron beam is located in the upstream beam tunnel. It is followed by a bremsstrahlung tagging spectrometer which occupies an enlarged tunnel section at the entrance of the hall. For tagged photon experiments, the primary electron beam is deflected downward into a low-power beam dump. Equipment to monitor the tagged photon beam – *e.g.*, a pair spectrometer and a total absorption counter – is located behind CLAS in the downstream tunnel section.

4.C.3 CLAS Performance

CLAS was commissioned in 1997, and started taking production data in December 1997. Major production runs were executed in the following categories:

- Electron scattering off hydrogen (e1 run group), deuterium (e1 and e5 runs), helium and nuclear targets (e2 run group); typically using a single-arm trigger on inclusive, scattered electrons; most runs done with polarized electrons.

- Tagged photons on hydrogen (g1 and g6 run groups), deuterium (g2 run group), helium (g3 run group); typically triggered on a single charged particle in CLAS in coincidence with the bremsstrahlung tagging system.

- Polarized electron scattering off solid-state polarized hydrogen and deuterium targets (eg1 run group).

The electron scattering experiments using CLAS have been typically conducted at a luminosity of 10^{34} cm^{-2}s^{-1}, slightly lower for a hydrogen target, slightly higher for deuterium and light nuclei. Tagged photon experiments were operated at around 10^7 tagged photons/s, typically limited by accidental coincidences between CLAS and the bremsstrahlung tagging system. The capabilities of the data-acquisition system have been steadily improved; data rates of 3,000 events/s and data throughput of 14 MB/s have been reached.

Angular coverage

Some fraction of the full solid angle is obstructed by the torus coils. Therefore, magnetic analysis is possible in the open gaps, only. Since the width of the torus coils is constant, the relative loss in ϕ-coverage increases with decreasing polar angle θ. Figure 78 shows the CLAS acceptance for full magnetic analysis of π^+ and π^- in the $(\theta - \phi)$ plane. Note that the acceptance depends on the charge of the particle, extending to smaller values of polar angle for the outward-bending (positive) particles.

Particle identification

Electron identification in CLAS relies on the combination of a signal from the threshold Čerenkov counter, as well as energy deposition in the electromagnetic calorimeter which matches the momentum as determined by the tracking chambers.

Neutral particles (photons and neutrons) are detected in the electromagnetic calorimeters (EC). The momentum and direction of photons are determined from the EC signals. The calorimeters provide photon energy measurements with a resolution $\sigma_E/E \leq 0.1/\sqrt{E(\mathrm{GeV})}$, and provide an angular resolution of ≤ 10 mrad. Mass determination for charged hadrons, π, K, p, and D, is accomplished by measuring the particle's momentum and velocity. The tracking chambers determine the track's momentum and path length, while the scintillator counters provide the time-of-flight measurement. As an example, Fig. 79 shows the mass distribution for charged particles produced in

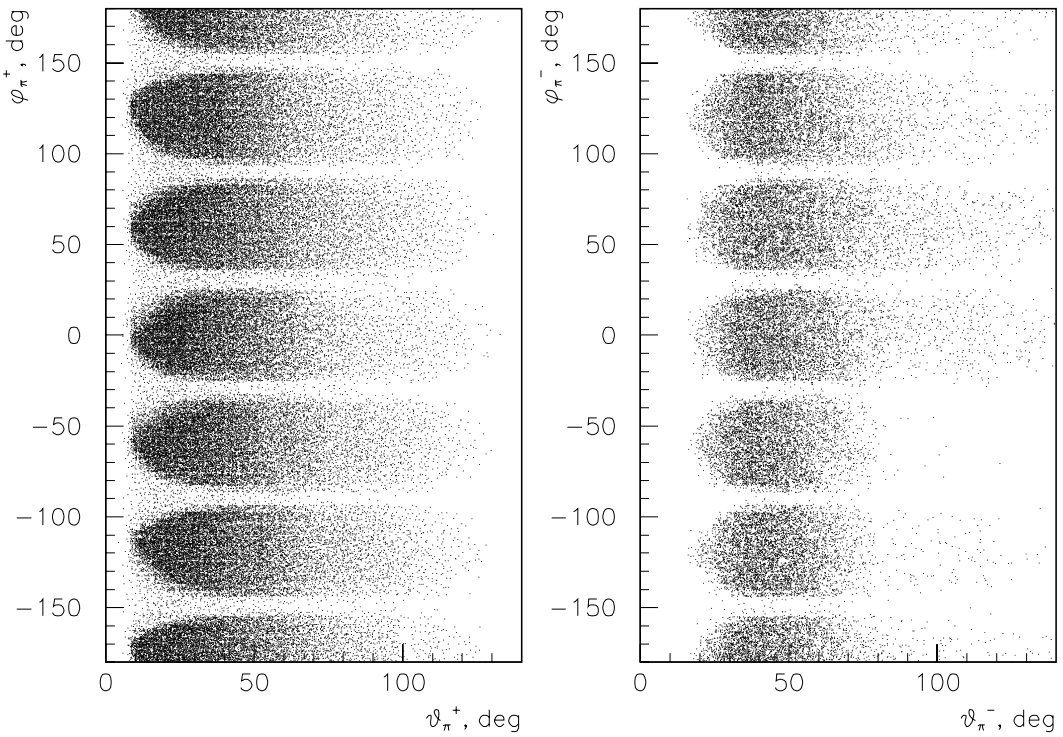

Figure 78: The angular acceptance if CLAS for π^+ (left) and π^- (right) plotted versus lab angles.

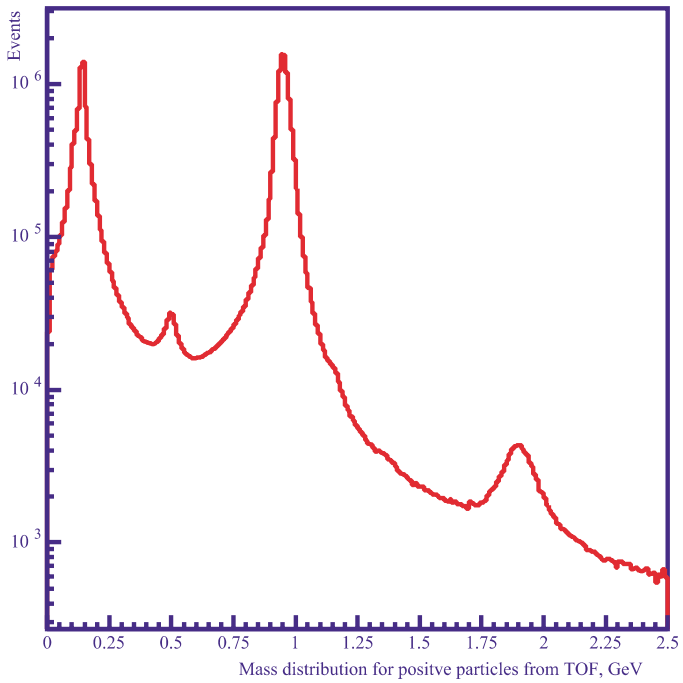

Figure 79: Mass distribution for charged particles produced in the $ep \to eX$ reaction at E_o = 2.4 GeV.

coincidence with electrons in the process $ep \to e'X$. The mass spectrum shows clear contributions from pions, kaons, and protons as well as a peak from deuterons.

Missing-mass technique

Much of the CLAS experimental program relies on the missing-mass technique to identify exclusive processes, especially for the identification of neutral particles in the final state such as:

$$ep \to ep\pi^0 \ , \ ep\eta, \ e\pi^+ n$$

or

$$\gamma p \to K^+\Lambda, \ K^+\Sigma^0, \ K^+\Lambda^*.$$

As an example, Fig. 80a shows the missing mass recoiling from the scattered electron and a π^+, showing the neutron and Delta peaks, while Fig. 80b shows the missing-mass distribution for the process $ep \to epX$. The missing-mass spectrum shows clear contributions from π^0, η, ρ, and ω production.

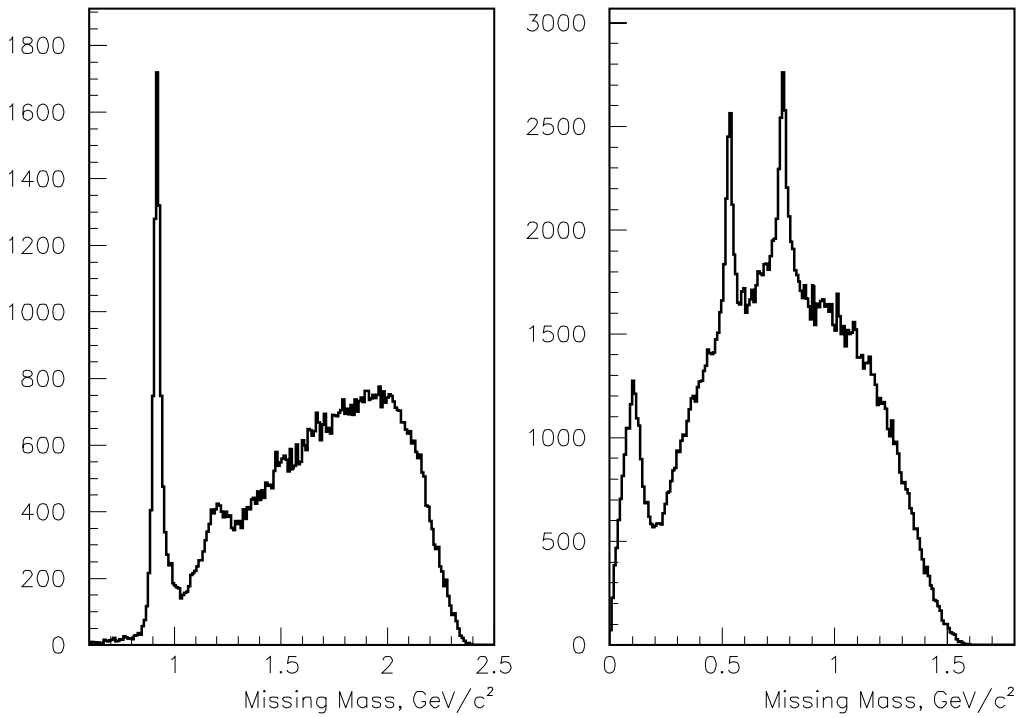

Figure 80: Missing-mass distribution for $ep \to e\pi^+X$ (left) and $ep \to epX$ (right) at $E_o = 4$ GeV.

4.C.4 Physics Program for an Upgraded CLAS

The main physics goal for an upgraded CLAS detector is a systematic investigation of exclusive scattering cross sections. The higher available beam energy will allow exclusive studies in unique kinematic ranges, for example, high-Q^2 studies of nucleon excitation, high-W studies of polarization transfer to hyperons, and a large range of formation time and distance in color-coherent studies, to name a few.

Among the most interesting studies are those in the Deep Exclusive Scattering (DES) regime, in which a forward meson is produced at small t but at large $Q^2$and W. These studies are expected to provide quantitative measures of the full quark wavefunctions (perpendicular as well as parallel momentum distributions) using the framework of the recently developed Generalized Parton Distribution (GPD) functions. (This is in contrast to deep inelastic inclusive measurements which give access only to the longitudinal momentum distribution.) To carry out this new DES program the following processes need to be investigated:

- Deeply virtual Compton scattering: $e\ p\ \rightarrow\ e'\ p\ \gamma$.
- Electroproduction of pseudoscalar mesons: $e\ p\ \rightarrow\ e'\ \pi^+\ n$ and $e\ p\ \rightarrow\ e'\ \pi^o\ p$.
- Electroproduction of vector mesons, in particular $e\ p\ \rightarrow\ e'\ \rho\ p$.
- Single-spin beam asymmetries in deeply virtual Compton scattering and target polarization asymmetries in pion production from protons.

The typical kinematic regime that needs to be covered is $W \geq 2$ GeV (to avoid the resonance region), $Q^2 \approx 2$ GeV/c^2 and higher, and small t.

In addition to the DES program, there will be logical extensions of the present CLAS program to higher masses for the final states, and to higher momentum transfers (see Ref. [Bu98] for details). Particularly important measurements are:

- The neutron form factor G_m^n to $Q^2 \approx 14$ (GeV/c)^2.
- Higher moments of spin structure functions; *i.e.*, determining $\int g(x, Q^2) \cdot x^n$.
- Flavor tagging of polarized spin structure functions.
- Meson transition form factors, *e.g.* $\omega \rightarrow \pi^0\gamma^*$, $A_2 \rightarrow \rho\pi$.

- Multi-nucleon knockout, and meson and N^* production and propagation in nuclei.
- Measurements of spin transfer from polarized electrons to hyperons at large W.
- Color coherent effects.

4.C.5 Design Goals for Higher Energy

The main goal of the CLAS upgrade is to maintain its capability to obtain high statistics data for exclusive electron scattering reactions at high energies. Many of the desired event samples (and the DES events in particular) form a medium-multiplicity (three to five final-state particles), low cross-section sample in a background of higher-multiplicity events. They are also typified by higher-momentum tracks emitted at smaller lab angles. A successful study of these exclusive reactions requires several major improvements in the CLAS's capabilities:

- The missing-mass technique needs to be augmented by a more complete detection of the hadronic final state.
- Efficient detection of the events requires complete photon reconstruction (energy and angle) over the complete azimuth for angles down to 5°.
- Similarly, partial charged track reconstuction (track identification and angle determination) is required over the full azimuth for angles greater than 5°.
- The luminosity of CLAS needs to be increased by about one order of magnitude over the present value to $L = 10^{35}$ cm^{-2} s^{-1}.

The small cross sections for the processes of interest mean that efficient background rejection is quite important. The primary backgrounds will likely be due to higher-multiplicity events with missing particles as well as events contaminated by out-of-time accidentals (not much of a problem at the present CLAS luminosity, but this will become important at 10^{35}). The primary strategy will be to positively identify the background, and to rely on missing-mass methods to pick out single, low-momentum particles (*e.g.*, recoil neutrons or slow π^-'s) that might otherwise escape detection. These requirements prescribe a more hermetic detector than the present CLAS as well as detectors capable of identifying that all particles came from the same event in both space and time.

Table 25 lists some of the characteristics of exclusive events at 12 GeV and the ensuing requirements for an efficient detector:

Table 25: CLAS upgrade plans: design goals

Event Characteristics	**Detector Requirements**
Higher multiplicity	More hermetic detector
	Good missing-mass resolution
Higher momentum	Easier electron identification
	π/p separation by TOF only to 3 GeV/c
Smaller lab angles	Move target back 1 m
Small cross sections	Better Møller shield
$\rightarrow$ high luminosity	Smaller sensitive time for wire chambers

4.C.6 CLAS Upgrade Plan

We will retain most of the present CLAS detector with the exception of the drift chambers, which will be replaced by new forward tracking chambers with smaller granularity. Moving the target upstream 1 m will enable particle detection down to 5°. Forward-going photons within the gap between torus coils will be detected by the EC counter; an auxilliary pre-radiator in front of the shower counter will improve the spatial resolution for photons. Forward tracking for charged particles in the inter-gap region will be accomplished by three stations of new drift chambers with smaller granularity. Special "gap" counters located in front of the main torus coils will restore full azimuthal coverage for forward-going photons and charged tracks, though full momentum reconstruction will be possible only for tracks penetrating the forward tracking stations. A central detector located within the superconducting solenoid will provide charged-particle tracking and photon detection for large-angle particles.

Table 26 recapitulates the design features required by the characteristics of DES events, and the new detector elements chosen to satisfy them. A conceptual design of the upgraded CLAS is shown in Fig. 81. The components of the upgrade plan will be discussed in more detail in the following sections.

Central detector

The dual need for more complete solid angle coverage as well as more robust shielding against the electromagnetic background of Møller electrons is satisfied with the addition of a new superconducting solenoidal magnet and associated central drift chamber and shower counters. This central

Table 26: CLAS upgrade plans: design choices

Requirement	**Design Element**
Better Møller shield Hermeticity requirement	Solenoid with central tracker and central calorimeter
Better missing-mass resolution Lower sensitive times	Tracking chambers with smaller cell sizes
Particle identification at higher momentum	Fine-grain pre-radiator before EC Use Čerenkov for pi/p separation
Smaller angle coverage	Move target back 1 m

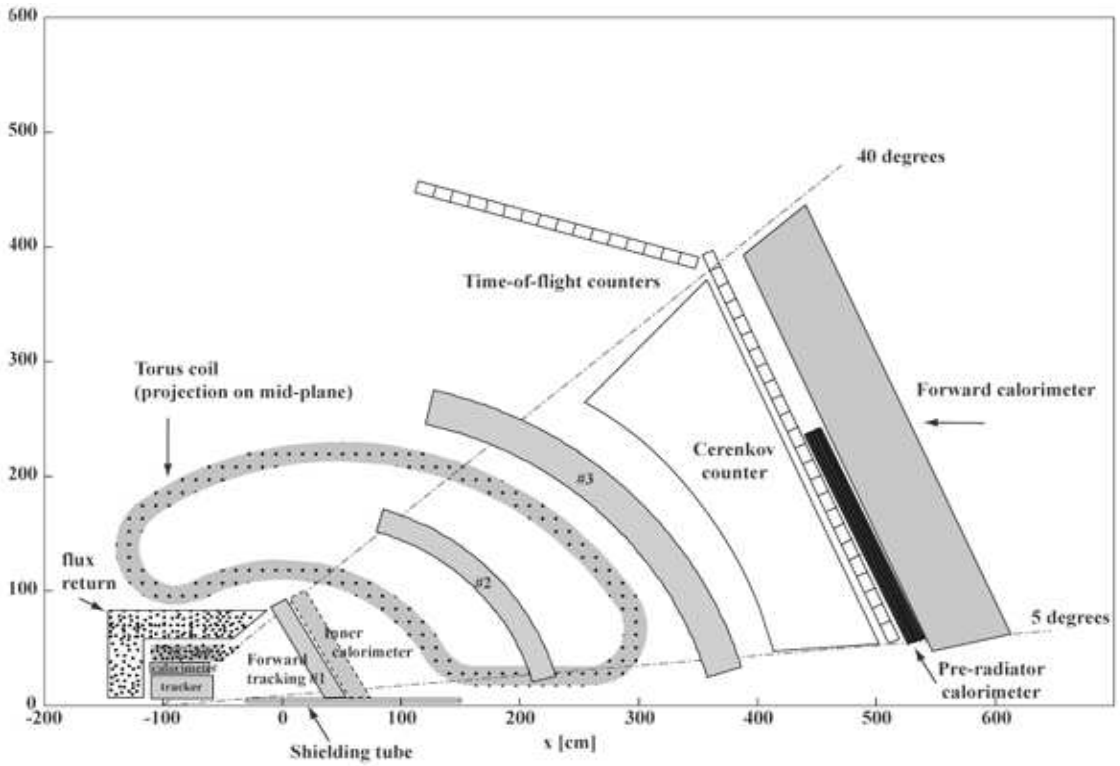

Figure 81: Conceptual view of the CLAS upgrade.

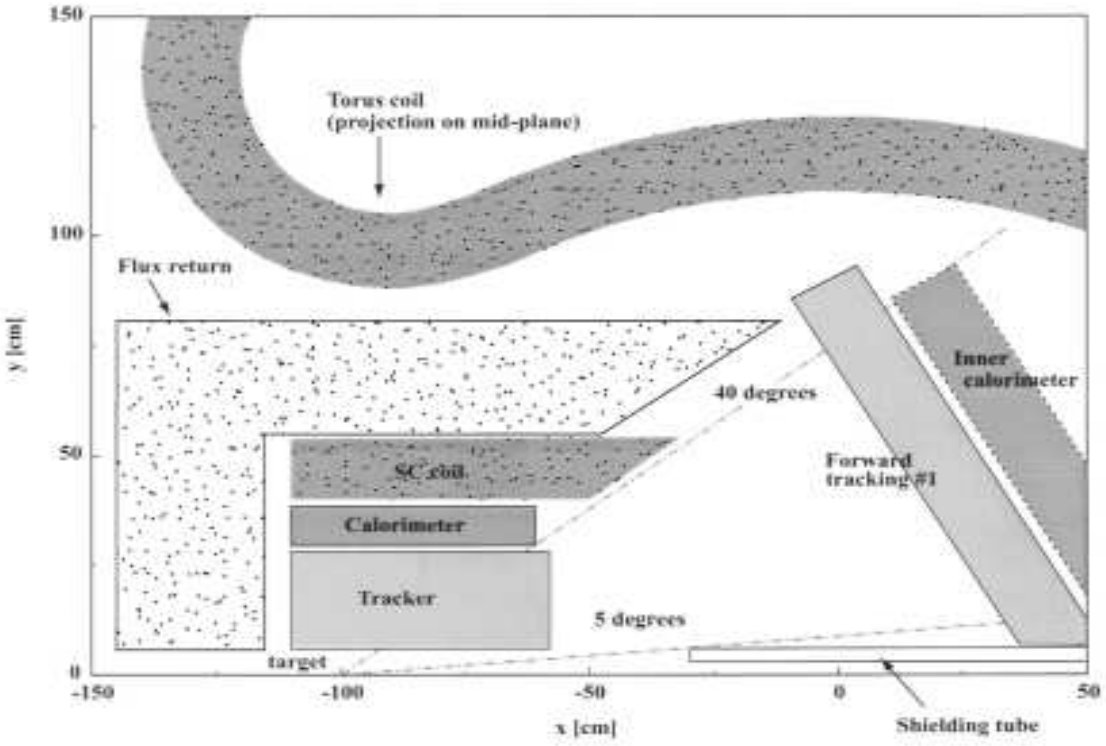

Figure 82: Conceptual view of the CLAS central detector.

detector (CD) allows the detection of charged and neutral tracks in the central region ($35^\circ \leq \theta \leq 120^\circ$) with a moderate fractional momentum resolution of $\delta p/p \approx 2\%$. A close-up view of the central detector is shown in Fig. 82. Note that the nominal target location has been shifted upstream by 1 m.

The detector uses a superconducting solenoid to provide a 1.5 – 5 T longitudinal magnetic field for the following functions:

- Keep Møller scattered electrons from reaching the detectors by guiding them along the magnetic field lines till they hit the inside of a heavy metal shielding pipe. This technique has been used successfully during the eg1 run, with the magnetic field provided by the 5 T polarized target magnet. This arrangement resulted in better shielding than the standard mini-torus magnet.

- Determine charged-particle momenta and charge via tracking in a central cylindrical drift chamber.

- Additionally provide the magnetic field for a solid-state dynamically polarized target. Polarized target operation adds homogeneity constraints which will require correction coils.

The flux return increases the field homogeneity and reduces the fringe field. Since shielding the Møller electrons relies on the fringe field the shaping of the flux return will be optimized for this purpose.

The central tracker uses gas-filled drift cells, either a standard drift chamber or straw tubes, to track charged particles over a radial distance of 25 cm. The expected transverse momentum resolution is $\delta p/p \approx 2\%$ (rms). A preliminary design uses an average cell radius of 3.5 mm, allowing three superlayers of wires of six layers each for a total of 18 wire layers. Each wire layer would have 180 wires in azimuth, yielding a total count of 3240 instrumented wires. Each wire will need a distance resolution of about 150 microns in order to achieve the desired 2% fractional momentum resolution. The expected hadronic accidental occupancy at a luminosity of 10^{35} cm^{-2}s^{-1} should only be about 0.5% per wire for a 100 ns time window. An interesting straw tube solution to a similar problem has been developed for the WASA detector at CELSIUS.

The function of the central calorimeter is to detect photons and neutrons, and to give some range information for charged particles (mainly to help identify recoiling protons). The calorimeter is located inside the coil and needs to be very compact to keep the coil diameter small. A promising construction technique that is presently being studied is to embed scintillating fibers into a high-density tungsten powder matrix. Another vital function of the central calorimeter is to determine the event time for all tracks in order to reject out-of-time accidentals.

Forward tracker

The small cross-sections expected for exclusive processes will require running at luminosities of $\approx 10^{35}$ cm^{-2}sec^{-1}. Sucessful use of the missing-mass technique at higher energy will also require better momentum resolution than the present detector for forward-going particles. We accomplish these two goals by redesigning our main drift chambers to have smaller cell sizes than the present chambers; this reduces the accidental occupancy by a factor of 4 (for tracks) or 8 (for isolated X-rays) and will also provide better position resolution and hence, better momentum resolution.

The resulting forward tracking system covers the angular range of 5–40 degrees for high-momentum particles. The proposed design uses three tracking stations located at the same positions as the present CLAS chambers. However, the angular range is smaller and the cell diameters are half the present size, yielding about the same total wire count.

Construction and mounting techniques are envisioned to be similar to the present drift chambers. The station 1 chambers will need to cover the full ϕ range; the goal, of course, being to detect as many tracks as possible from the high-multiplicity events, even if we don't measure the momentum accurately, in order to veto these events. To achieve this full coverage in azimuth for the station 1 chambers we plan to build six independent trapezoidal chambers with light-weight frames coupled mechanically to support the wire tension (analogous to our present Region 1 chambers).

The dead area of the station 1 tracking chambers will covered by six additional (narrow) rectangular chambers, referred to as the "gap" chambers. The detectors in this "gap" area are covered in the next section.

GAP detectors

In the present CLAS detector, charged or neutral particles heading for the coils are not detected. One would like to determine the directions and make a coarse energy measurement for all photons, and to determine the direction for charged tracks in this region. This requires instrumenting the inside of the torus coils with the so-called inner photon detectors and the "gap" tracking chambers.

The gap chambers must not intrude into the intra-coil region for which the forward tracker will measure momentum. It must also measure accurately the radial coordinate in order to measure the angle (but not the charge or momentum) of track segments. One concept is to have radial wires with the signals picked up by azimuthal cathode strips. An alternate strategy has wires running azimuthally with only low-profile capacitors in the sensitive region and the pre-amplifiers and signal cables hidden behind the chambers.

The inner photon detector will have to be very compact since there is little space available. Ideally, the detector should also give some information on charged particles, like energy deposition, range, etc. A possible solution is to install short-radiation-length crystals (*e.g.*, lead tungstate) in the angular range between 5° and 45° to complement the forward calorimeters (see Ref. [Bu98a] for more details). An important open question is the choice of the readout technique.

Particle identification strategy

For e/π separation the present technique of combining energy deposition in the calorimeter and a signal in the Čerenkov counter will be limited to $p \leq 2.7$ GeV/c since the Čerenkov counters will

record pion events at the higher operating energies. The solution is to rely on the electromagnetic calorimeter alone for e/π separation. The relative calorimeter resolution improves with increasing energy; in addition, one can make better use of the longitudinal and transverse energy deposition patterns, which are different for e and π.

Typical exclusive events at high energy will naturally have higher-momentum particles than those in present experiments, making particle identification more difficult. To study DES adequately, we will need to extend π/p separation up to 6 or 8 GeV/c. Pion-proton separation by time of flight works up to about 3 GeV/c momentum. Pions with higher momenta give a signal in the Čerenkov counter, distinguishing them from protons. Kaon-pion separation can likewise be accomplished up to 2 GeV/c by time of flight, and above 3 GeV/c by using the Čerenkov counter to indicate a pion. There will be a gap in positive kaon-pion separation between 2 and 3 GeV/c momentum. We plan to accomplish effective kaon identification in this range by using constrained fitting, or in some cases, by detecting the hyperon directly. We can also enhance our detection of the weakly decaying strange particles by detection of a detached vertex.

The position resolution of the present electromagnetic calorimeter (EC) is insufficient to separate single photons (*e.g.* from the DVCS process) from two photons from the decay of high-momentum π^0's since the half-angle of photons from the decay of an 8 GeV/c π^0 is less than 1^0. The two-photon separation will be enhanced by adding a smaller-granularity, four-radiation-lengths pre-shower calorimeter in front of the existing EC. Using the same lead-scintillator sandwich construction technique as for the EC, but with scintillator strips of half the width, will give the desired position resolution. Since the maximum π^0 energy falls steeply with increasing polar angle, only half of the forward calorimeter face needs to be covered by the pre-shower radiator. The new detector elements necessary to complete the upgrade are listed in Table 27.

Trigger and data acquisition

Triggering at high energy will be challenging since the Čerenkov counters will be less effective in enriching the event sample with electrons. At a luminosity of 10^{35} cm^{-2}s^{-1} the total hadronic production rate is about 10^7s^{-1}. Assuming a data-acquisition capability of 5,000/s, the trigger has to provide a factor of 2000 rejection of hadronic events. The following requirements will be used in the Level I and II trigger:

- High energy in the calorimeter, with independent thresholds in the front and rear elements.
- Matching signal in the Čerenkov counter, which will eliminate contributions from high-energy

Table 27: CLAS upgrade plans: new detector elements

New Detector	**Description, Expected Performance**
Central solenoid	Superconducting, 1 m diameter, 0.5 m length, up to 5 T field for tracking, Møller shield
Central tracker	Cylindrical chamber, 18 layers × 180 wires stereo and axial wires, 150 μm accuracy
Central calorimeter	Lead tungstate, $10\%/\sqrt{E}$ energy resolution
Inner calorimeter	Lead tungstate, covers coil faces
Gap tracker	Finds track segments, determines track angle Covers coil face
Forward tracker	3 regions of drift chambers with small granularity Same coverage as present DC's, twice the granularity
EC pre-radiator	Covers inner angular range of EC's Gives better spatial resolution for photons

photons hitting the calorimeter.

- Negative polarity track matching the energy deposition in the calorimeter.

On-line event analysis in a Level III trigger will reduce further the number of events that have to be written to tape.

Bremsstrahlung tagging system

The present bremsstrahlung tagging system is limited to $E_o \leq 7$ GeV by the requirement to bend the primary electron beam into the 30° dump line. The present plan is that tagged photon experiments at higher energies will generally be performed in Hall D.

We have considered ways to upgrade the maximum energy of the tagging system by using alternative beam dumping schemes. We are also investigating possible ways to detect and trigger on very small-angle scattered electrons in coincidence with a hadronic event, providing tagged photons with $Q^2 \approx 0$. For now, we have no plans to upgrade the tagging system.

Expected performance: CLAS upgraded detector We have done some simple simulations of various components of the CLAS upgrade under expected experimental conditions. We

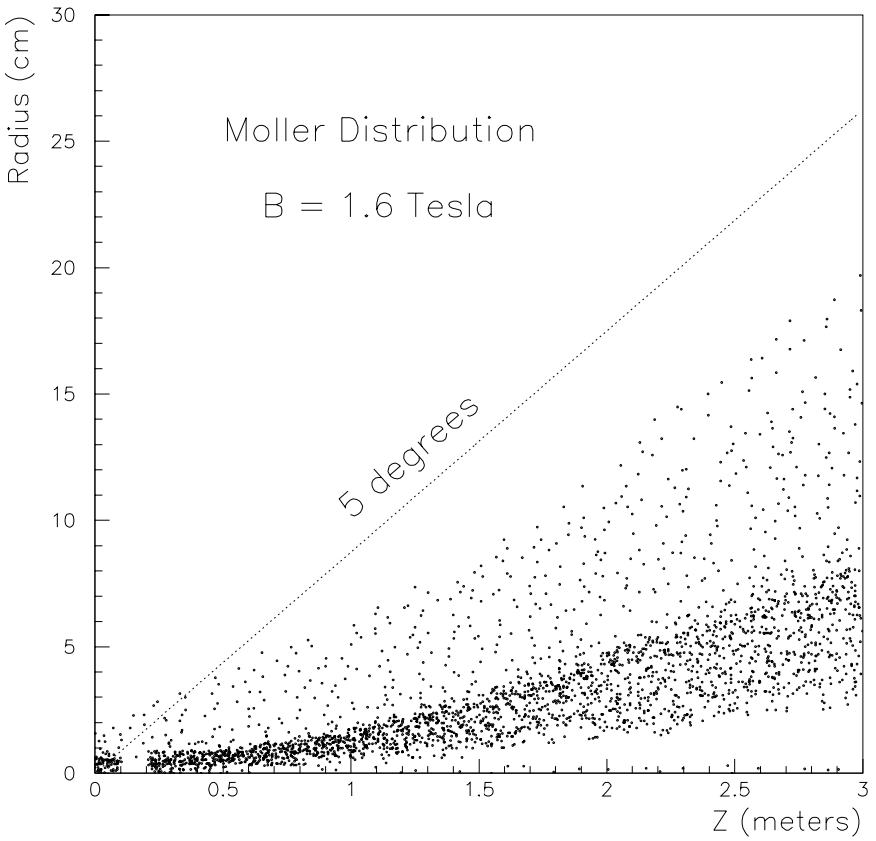

Figure 83: Møller flux rate as a function of the z coordinate along the beam versus the radial position. A 5° line is shown for comparison.

have broadly specified the size and current density of the central solenoid by considering its effect on the expected flux of Møller electrons from the target. The strategy is to confine the Møllers to widening spiral trajectories using the solenoid's magnetic flux lines, and to absorb these electrons when they strike the inner face of a cylindrical shielding tube. We note that this shielding technique has been successfully used in the EG1 experiments in the present CLAS setup.

In Fig. 83 we plot the expected flux density of Møller electrons as a function of the z coordinate along the beam line in meters and the radial coordinate in centimeters. The shielding of the Møller electrons for this study is accomplished by a 1-m-diameter and 0.5-m-long solenoid with a maximum field strength of 1.6 T. Note that for z positions greater than about 0.5 m, all Møllers are confined to a cone smaller than 5°. For higher B fields, the cone angle is smaller still.

We have estimated the resolution for the perpendicular momentum component of charged

Table 28: CLAS upgrade plans: expected performance

	Resolution		
Component	**Spatial**	**Time**	**Energy**
Central tracker	150 microns/layer	na	na
Central calorimeter	10 cm	1 ns	10%
Gap calorimeter	10 cm	1 ns	10%
Gap tracker	100 microns	na	na
Fwd. tracker	150 microns/layer	na	na
TOF banks	1 cm	100 ps	na
EC (with pre-radiator)	5 cm	1 ns	5%

particles traversing the CD's drift chamber by dividing the expected spatial accuracy (150 microns per layer) by the sagitta of a charged track traversing a solenoidal field. We obtain an estimate of $\delta p/p = 2\%$. Likewise we estimate that new EC with preceding pre-radiator should be able to achieve the same energy resolution as the present EC, that is $\approx 7\%/\sqrt{E}$, but should have much better position accuracy, down to an uncertainty of only 1 cm. Table 28 lists the individual detector components and their expected resolution in position, time, and energy where applicable.

Since the missing-mass technique will be employed to identify exclusive events with a missing recoil neutron from, for example, a recoil delta baryon, we have simulated the momentum and angular resolution of the forward tracking system to see what spatial resolution is required. Fig. 84 shows a plot of the missing mass recoiling from the scattered electron and forward-produced pion in $ep \rightarrow e'\pi^+(N)$ events. These events were simulated with a beam energy of 11 GeV. Overplotted are two spectra, obtained from assuming that the tracking chambers have 100 and 400 micron accuracy, respectively.

4.C.7 Hall B Summary

The planned Hall B physics program at 12 GeV requires an upgraded CLAS detector which has better magnetic shielding, more complete angular coverage, better momentum resolution in the forward tracking region, smaller time windows in the tracking system, and coverage down to smaller polar angles than the present detector. We accomplish these design goals by: adding a central solenoidal magnet instrumented with a cylindrical drift chamber and inner shower counter (to provide hermetic coverage of slow recoil particles while giving good magnetic shielding for Møller electrons); replacing the current tracking system by three stations of forward tracking chambers

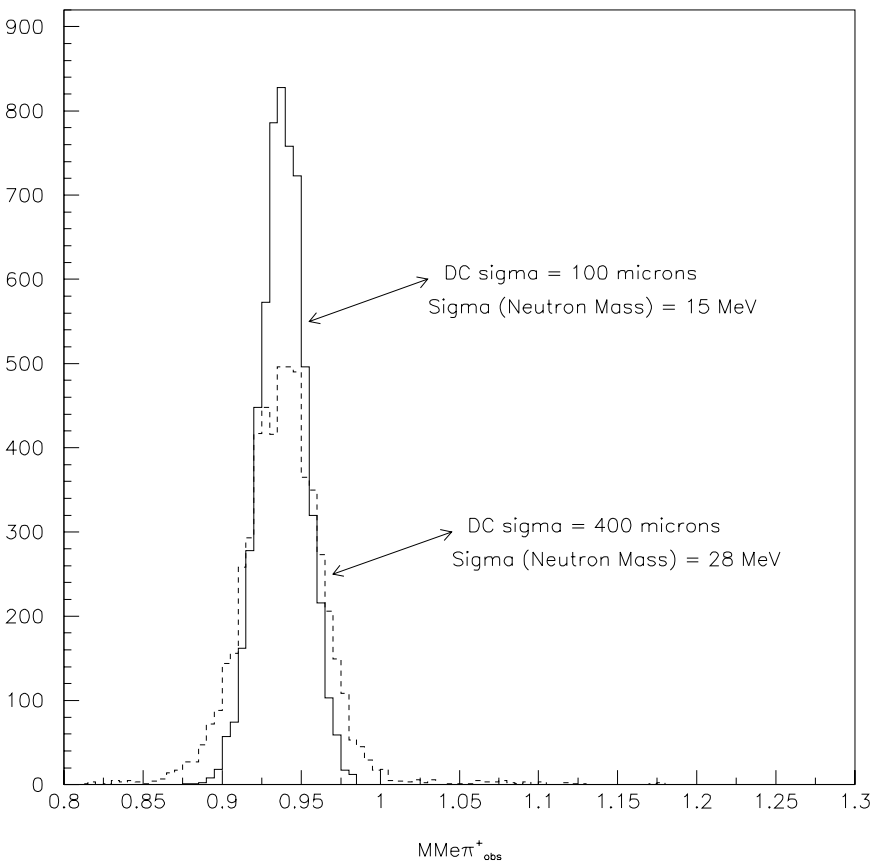

Figure 84: Simulated missing mass for the reaction $ep \rightarrow e'\pi^+N$.

(which have half the cell size and hence, lower sensitive time and better resolution, than the present system); augmenting the electromagnetic calorimeters with a fine-grained pre-radiator; and moving the target position back a meter to gain access to tracks with polar angles down to 5°.

These changes should allow the efficient detection of exclusive events, representing the majority of the planned program, at luminosities up to 10^{35} $\mathrm{cm}^{-2}\mathrm{sec}^{-1}$. With these changes, the exciting program of investigating Deep Exclusive Scattering and thereby beginning the next-generation studies of the nucleon's quark wavefunction should be within our experimental grasp.

4.D Hall C

Hall C at Jefferson Lab has generally been used for experiments which require high luminosity and good resolution. Since the beginning of operations at JLab, the core spectrometers have been the High-Momentum Spectrometer (HMS) and the Short-Orbit Spectrometer (SOS). These two devices have been used flexibly in the experimental program as either electron or hadron arms, in coincidence with one another or with a third user-supplied arm. The HMS has $P_{\rm max} = 7.6$ GeV/c and is compatible with the 12 GeV Upgrade, but the SOS has only a limited maximum momentum of 1.7 GeV/c. The HMS will be in need of a new, high-momentum companion spectrometer: the Super-High-Momentum Spectrometer (SHMS), which will have the flexibility and dynamic range to carry out a broad physics program.

4.D.1 Overview

The Super-High-Momentum Spectrometer (SHMS) will play a vital role in the overall JLab physics program at 12 GeV. An inevitable consequence of relativistic kinematics is that much of the interesting physics at 12 GeV will only be accessible provided at least one of the spectrometers can achieve angles significantly below 10°. The SHMS will achieve a minimum scattering angle of 5.5° with acceptable solid angle and do so at high luminosity. The maximum momentum will be 11 GeV/c, well matched to the maximum beam energy available in Hall C. These three characteristics (high luminosity, small scattering angle, and high momentum) are essential for carrying out a program of electron-hadron coincidence experiments at large $z = E_h/\nu$ where ν is the electron energy loss. (For orientation, in the limit of $z \to 1$, one approaches the exclusive limit.) At large z (*i.e.*, $z \simeq 1$), sensitivity to the valence quark structure of the hadron is maximized and the reaction mechanism is simplified. The HMS-SHMS spectrometer pair will be rigidly connected to a central pivot which permits both rapid, remote angle changes and reproducible rotation characteristics which simplify accurate measurements. From its inception, the SHMS momentum and target acceptances were designed to be very flat, with similar performance to the HMS, which also will greatly simplify making accurate measurements. Finally, for experiments which are willing to trade off small-angle performance for increased solid angle, this can be achieved by pulling the first two quads forward and retuning the spectrometer. In the remainder of this section we will discuss several physics examples which drive the SHMS requirements.

Measurements of the charged pion form factor at large Q^2

The long-term interest in this subject is due to the calculation of Farrar and Jackson [Fa75], who showed that the pion form factor (F_π) is rigorously calculable in pQCD at asymptotic values of Q^2. Such a rigorous prediction is almost unique in QCD. However, for the finite values of Q^2 where experiments are actually performed, the situation is more complex. Nonperturbative "soft scattering" contributions must be explicitly taken into account. After years of theoretical effort, there has been considerable progress in our understanding of the smallest value of Q^2 for which the hard scattering amplitude may dominate (*e.g.*, [Is84, Ja90, Ti92, It92, Ja93, Mu95, Do97]). The pion is the laboratory of choice for these studies because the smaller number of valence quarks in the pion means that the asymptotic regime will be reached at lower values of Q^2 for F_π than for the nucleon form factors. Thus the pion "laboratory" may eventually provide the same level of insight into light-quark QCD that the deuteron "laboratory" has provided for studies with nucleon and meson degrees of freedom.

The high-quality, continuous electron beam of Jefferson Lab makes it the only place to seriously pursue these measurements. Completed JLab experiment 93-021 explored F_π to $Q^2 = 1.6$ with 4 GeV beam using the HMS-SOS combination in Hall C. However, a serious test of QCD-based models requires the construction of the SHMS and the 12 GeV electron beam Upgrade. The reaction used is exclusive $p(e, e'\pi^+)n$ and the longitudinal response function $d\sigma/dt$ must be isolated via a Rosenbluth separation. The most stringent requirement this experiment imposes upon the SHMS design is the 5.5° forward angle capability. An accurate and reproducible coupling to the present pivot is also needed, as well as relatively flat acceptances in phase space. Figure 40 shows the size of the anticipated error bars with the SHMS+HMS combination and 12 GeV beam. It is easily seen that the JLab Upgrade would allow a dramatic advance in the understanding of the pion form factor.

Color transparency

The Color Transparency (CT) conjecture by Mueller and Brodsky [Mu83] has stimulated great interest. CT was first discussed in terms of perturbative QCD considerations. However, later work [Fr92a] indicated that this phenomenon occurs in a wide variety of situations with nonperturbative reaction mechanisms. The existence of CT requires that high-momentum-transfer scattering take place via selection of amplitudes in the initial- and final-state hadrons characterized by a small transverse size. Furthermore, this small object should be "color neutral" outside of this small radius in order not to radiate gluons. Finally, this compact size must be maintained for some

distance in traversing the nuclear medium. Unambiguous observation of CT would provide a new means to study the strong interaction in nuclei.

Jefferson Lab has several advantages to offer in searching for CT effects via quasielastic $A(e,e'p)$ measurements. First, data from experiments NE18 at SLAC [Ma94] and completed JLab experiments E91-013 [Ab98] and E94-139 will provide a baseline for conventional Glauber calculations. Second, the fundamental electron-proton scattering cross section is smoothly varying and accurately known in this kinematic range. Finally, the high duty factor, high luminosity, and large solid angle of the high-momentum Hall C spectrometers all contribute to making high-quality, precision measurements feasible.

Upgrading to a 12 GeV beam energy would allow measurements at even higher momentum transfers. With the planned Hall C upgrades a momentum transfer of about 18 $(\mathrm{GeV}/c)^2$ could be obtained. The most stringent requirement this experiment places on the SHMS design is that the proton momenta approach the beam momentum, so a reasonable maximum SHMS momentum is 11 GeV/c. In Fig. 49 we show an overview of previous results from nuclear transparency measurements in combination with the projected uncertainty using the HMS-SHMS combination for the $^{12}\mathrm{C}(e,e'p)$ reaction. The highest Q^2 point assumes a data-taking period of 80 hours. As shown, such a precise data set will allow us to distinguish between conventional Glauber calculations and the state-of-the-art CT predictions of Nikolaev *et al.* (CT(I); Ref. [Ni94]) and Frankfurt *et al.* (CT(II); Ref. [Fr94]).

$N \rightarrow N^*$ form factors at high Q^2

The upgraded Hall C will have a unique role to play in studies of neutral meson electroproduction at high Q^2. As in the completed JLab experiment 94-014, high-Q^2 studies of the resonant amplitudes of the $\Delta(1232)$ and $S_{11}(1535)$ via $e+p \rightarrow \Delta(1232) \rightarrow p+\pi^0$ and $e+p \rightarrow S_{11}(1535) \rightarrow p+\eta$, respectively, can be executed (Fig. 39). For the single meson decay channel, measuring only one of the decay hadrons completely determines the kinematics of the entire reaction, including the other undetected hadron. In particular, the neutral single meson is identified by the missing mass of the detected proton and electron, and its CM kinematics by missing momentum. An important property of high-Q^2 reactions which Hall C can take advantage of is that the hadronic reaction products are boosted into a narrow cone relative to the momentum transfer, so that large CM angular acceptances in θ and ϕ can be obtained with relatively modest angular-acceptance spectrometers. This is especially true for the recoil protons in single neutral meson production, $p(e,e'p)\pi^0$ and $p(e,e'p)\eta$. The protons emerge in a narrow cone around the momentum transfer $\vec{q}$. For example, if

we consider π^0 production at the delta peak, $W = 1232$ MeV, at $Q^2 = 10$ (GeV/c)^2 the cone angle in the lab corresponding to 4π in the CM is 2.7° (47 mr). For η's at the peak of the $S_{11}(1535)$ resonance the angle is 2.5° (43 mr). With modest solid angle acceptance spectrometers one can obtain almost all of the decay proton cone, and then select the π^0 and η channels by reconstructing their missing mass.

In experiment 94-014 the HMS detected the protons with momenta up to about 3.5 GeV/c, and the SOS detected the scattered electrons with a momentum about 1.5 GeV/c. At much higher Q^2 [*e.g.*, ~ 15 (GeV/c)^2], the SOS must be replaced by a new spectrometer, the SHMS. At these increased Q^2 both spectrometers must have high maximum-momentum capabilities. In addition *both* must have adequate resolution ($\simeq 0.1\%$ in momentum and $\simeq 1$ msr in θ and ϕ) and adequate solid angle.

Duality and fragmentation

In the early 1970s Bloom and Gilman made the phenomenological observation that there is a duality between electron-proton scattering in the resonance and in the deep inelastic regions [Bl70]. Duality in this situation means that resonance bumps observed in the structure functions at low Q^2 average out to mimic the smooth scaling functions measured at higher Q^2. This implies that the single-quark scattering process determines the scale of the reaction, even in the nucleon resonance region, provided one averages over a suitably wide region of kinematics. Bloom-Gilman duality has recently been verified to hold to high precision down to very small values of Q^2 [$<$ 1 (GeV/c)^2] [Ni99]. This last observation, if reliably understood, could allow one to use duality to study structure functions in hitherto difficult to access kinematics regions, *e.g.*, the region of Bjorken $x \to 1$.

Carlson *et al.* have argued that duality should also hold in the longitudinal structure function for inclusive scattering, and in pion photoproduction for semi-exclusive scattering [Ca90, Af00]. Related to the latter case may be semi-exclusive deep inelastic scattering with parallel kinematics. Here duality would manifest itself with an observed scaling in the meson plus resonance final state. Assuming one is in a kinematic region that mimics single-quark scattering, in analogy to the inclusive case, the question here is whether the remaining part of the process can be described as hadronization of the struck quark into the detected meson. In such a factorization approach, the cross section decomposes into a part dependent on the photon-quark interaction and an independent part on the quark fragmentation functions $D^h_{q_i}$ (or the probabilities that a quark of flavor q_i hadronizes into a hadron h).

One would assume this factorization to be strictly valid at asymptotic energies only; however, similar to the inclusive case where the nucleon resonances quickly heal to the scaling curve, here the conspiracy of the nucleon resonances remaining in the final state after having produced a fast meson may heal to a fragmentation function. A pictorial example is given in Fig. 43. Data of HERMES and JLab seem to indicate that the factorization assumption works at lower than asymptotic energies, provided one additionally makes a cut in z [Ac98, Mkpc].

For $\pi^{\pm}$ and $K^{\pm}$ electroproduction at large $z = E_h/\nu$, it is essential that the hadron arm accesses angles of about 6°. This will enable us to test meson duality, and, if also quantified, access fragmentation functions and parton distribution functions through a flavor decomposition in hitherto inaccessible regions. The HMS-SHMS combination fully exploits the high-luminosity 12 GeV energy domain here!

4.D.2 SHMS Optical Design

The design of the SHMS was primarily driven by the needs of the coincidence physics program described briefly above. Happily, the resulting constraints resulted in a buildable device with enough flexibility to carry out a broader physics program, including many other experiments described in detail in Chapter 2.

Here we list the constraints on the SHMS design. The first five are hard, imposed by the physics objectives (in parentheses). The next two constraints match the SHMS to the existing HMS:

- Maximum momentum of 11 GeV/c (CT, $N \to N^*$).
- Minimum central angle of 5.5° (pion form factor, fragmentation).
- Maximum angle of 30° ($N \to N^*$).
- Moderate resolutions in momentum ($\simeq 0.1\%$) and angle ($\simeq$ 1 mrad).
- Moderate solid angle (2–3 msr in small-angle mode).
- Full acceptance of a 15 cm cryotarget cell at $\Theta_{\rm SHMS} = 30°$ (*i.e.*, $Y_{\rm tar} = \pm$ 3.75 cm).
- Minimum opening angle of the SHMS-HMS pair to be $5.5° + 10.5° = 16°$.
- Distance to the focal plane less than 19 m.

- Bend angle of the dipole larger than 15° (no line of sight to target!).
- Larger vertical than horizontal angular acceptance.

The final three constraints in the list are imposed to leave sufficient space for detectors and shielding, prevent single-scattering events from reaching the focal plane, and emphasize coverage in the out-of-plane angle ϕ essential for interpreting $(e, e'h)$ measurements. For convenience in commissioning we employ a point-to-point tune. To simplify the design and procurement effort the two first quadrupoles are taken to be HMS Q1-type, which have a horizontally slim design and maximum gradient of 8.4 T/m.

We have arrived at a magnetic optical design for the SHMS that fulfills all of the above constraints and preferences. The design consists of two superconducting quadrupoles and one combined-function magnet consisting of a dipole-quadrupole combination (DQ). The DQ magnet consists of a $\cos(\Theta)$ dipole and a concentric $\cos(2\Theta)$ quadrupole. The third quadrupole element, located inside the dipole, is needed to obtain a larger vertical than horizontal angular acceptance in combination with the moderate-resolution requirement. (Recall that both the HMS and HRS spectrometers employ a Q^3D design.) Combining the dipole and third quadrupole element into a single package also makes the total spectrometer shorter.

We have modeled the combined-function (DQ) magnet in COSY by incorporating the TOSCA field map calculation. COSY is used to provide the forward and reconstruction matrix element sets to fifth order, which are then used in a FORTRAN Monte Carlo simulation of the SHMS spectrometer including finite resolution position measurements in twelve wire chamber planes and multiple scattering in all the windows and detector elements. The size of the beam envelope in the dispersive (x) and nondispersive (y) directions is given in Fig. 85.

Typical resolutions in the reconstructed target quantities (δ, $\phi \equiv dx/dz$, $Y_{\rm tar}$, and $\theta \equiv dy/dz$) are shown in Fig. 86 as a function of $\delta \equiv (p-p_0)/p_0$ for a 2.5 GeV/c electron. This is obviously at the low end of operations for an 11 GeV/c spectrometer, and so nearly worst case, but it demonstrates the flexibility of the SHMS. The solid curves are our best estimate of the real-world resolutions under conditions which are far from ideal. The dashed curves neglect multiple scattering and demonstrate the importance of including this effect. The dot-dash curves further neglect the finite resolution of (very conservatively) 150 μm per wire-chamber plane, thus demonstrating the ultimate resolution when the optics are limited to fifth order. At higher momenta (*e.g.*, 7.5 GeV/c), some experiments requiring good $e^- - \pi$ discrimination will install a long, low-pressure gas Čerenkov which must go before the drift chambers due to space constraints. Despite the additional material before the

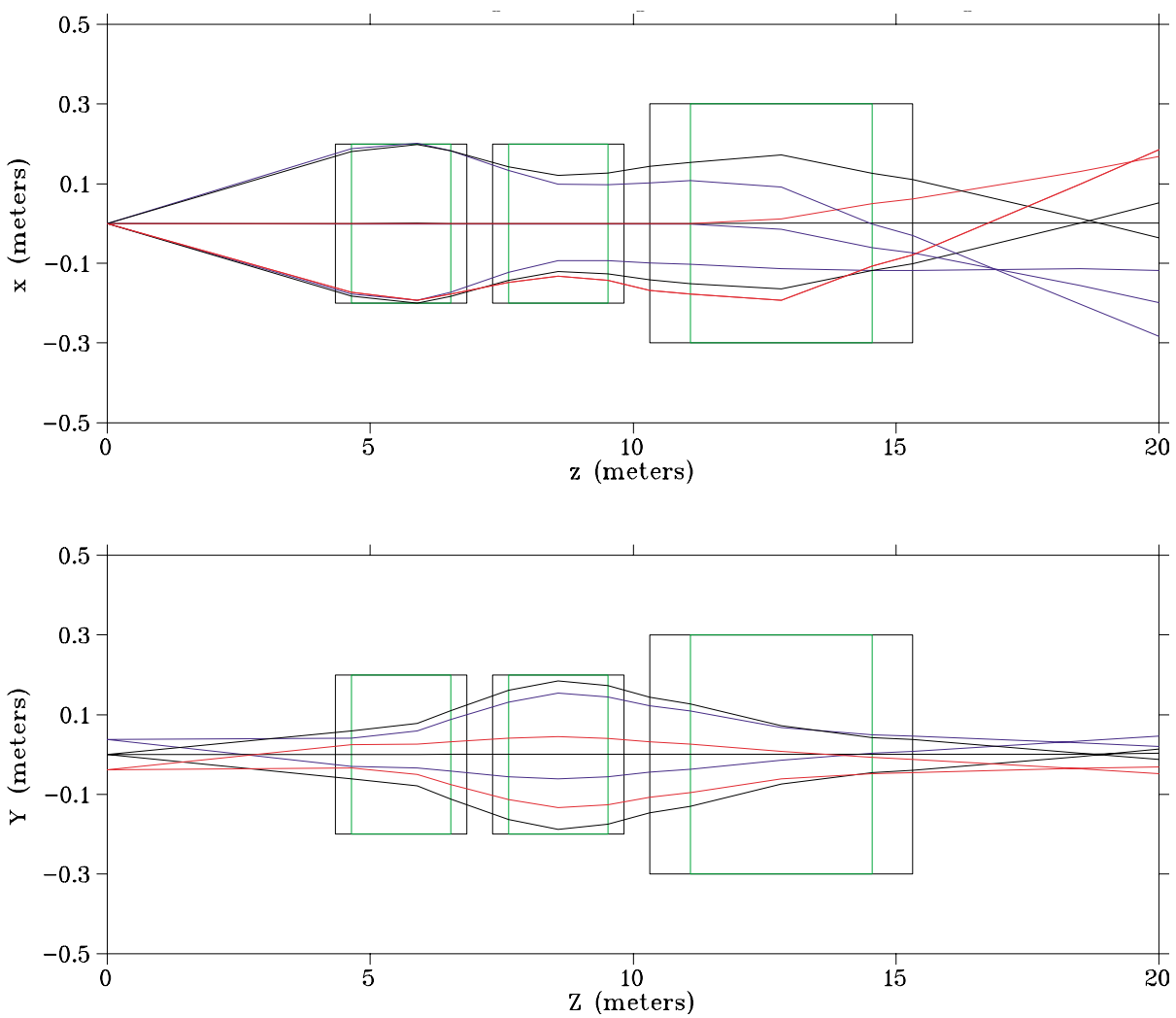

Figure 85: Beam envelopes through the SHMS in the dispersive (upper figure) and nondispersive (lower figure) planes. In the dispersive direction, rays were generated for $\delta = 0, \pm 10\%$. In the transverse direction, rays were generated for $Y_{\rm tar} = 0, \pm 3.75$ cm.

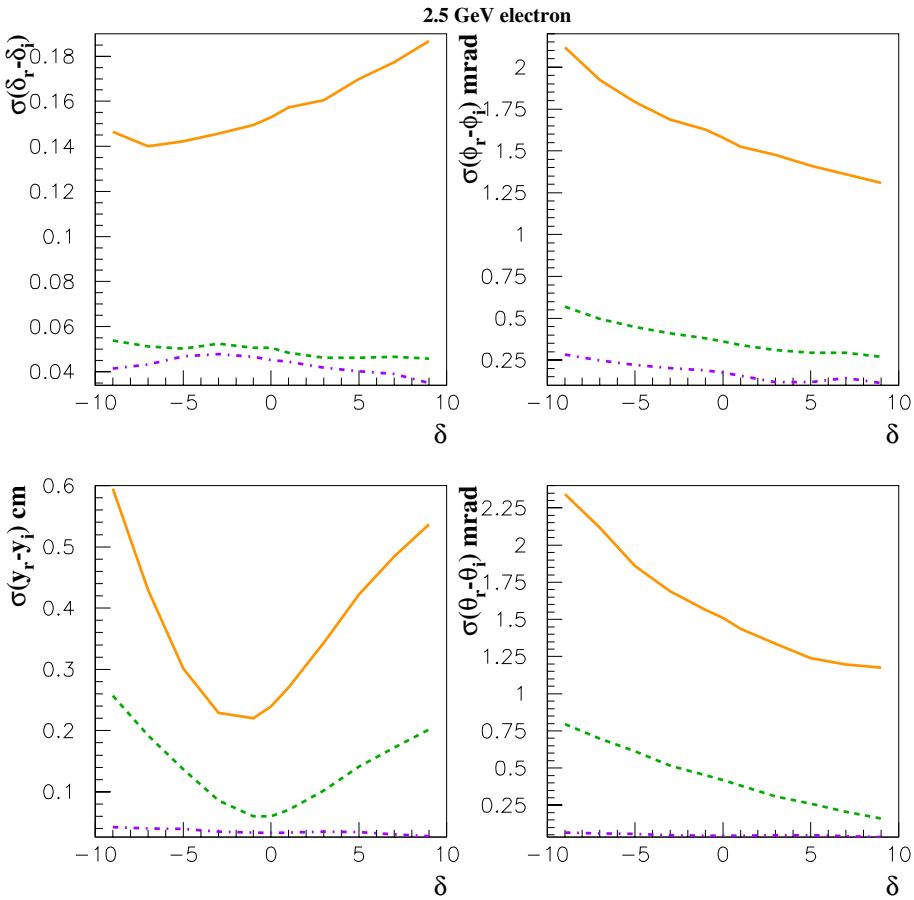

Figure 86: Typical resolutions in the reconstructed target quantities (δ, ϕ, Y_{tar}, and θ) are shown as a function of $\delta \equiv (p - p_0)/p_0$ for a 2.5 GeV/c electron. The solid curves are our best estimate of the real-world resolutions. See text for a detailed explanation of the other curves.

Table 29: The basic parameters of the SHMS; resolutions are quoted for 2.5 GeV/c electrons.

Max. central momentum	11 GeV/c
Min. scattering angle	5.5°
Momentum resolution	0.15%–0.2%
Xptar,yptar resolution	1–2 mrad, 1–2 mrad
Ytar resolution	0.2–0.6 cm
Vertical acceptance	±42 mrad
Horizontal acceptance	±14 mrad
Solid angle	2 msr (small angle mode)
Momentum acceptance	20%
Opening angle with HMS	16°
Configuration	QQ(DQ)
Bend angle	18.4°
Focusing mode	Double
Max. rigidity	400 kG-m
Dispersion	1.764 cm/%
D/M	1.20 cm/%
Mx	1.47
My	1.02
Focal plane angle	4.88°
Focal plane dimension	40 cm (X) × 20 cm (Y)
Optical length	18.5 m

drift chambers, the reduction in multiple scattering means that the resolutions are comparable to or better than those in Fig. 86. The basic parameters of the SHMS of primary concern to experimentalists are summarized in Table 29.

4.D.3 Magnet Engineering

The SHMS requires a combined-function superconducting magnet that can simultaneously produce 4.0 T dipole fields and a 3.0 T/m quadrupole field inside a warm bore of 30 cm. A magnetic design using TOSCA 3D has been performed to establish the basic magnetic requirements, to provide three-dimensional field maps for optics analysis, and to produce basic engineering information about the magnets. A four-sector $\cos(\theta)$ current distribution and a two-sector $\cos(2\theta)$ quad design with warm bore and warm iron have been analyzed. A cutaway view of the combined-function dipole DQ is seen in Fig. 87. The basic parameters of the DQ are given in Table 30.

The yoke is modeled as truly nonlinear iron with the nominal properties of 1006 steel. The present design yoke is 4.2 m long with an outer elliptical shape with semi-major and minor radii of 120 cm by 100 cm and a cylindrical bore with a 60 cm inside radius. The yoke has been optimized

to achieve a 5.5° scattering angle at fields capable of 11 GeV/c. The detailed shape of the yoke is less important in a cosine-type magnet as the design requires an unsaturated yoke for good internal fields. The high-field region is either on top or on the bottom depending on the relative sign of the dipole and quadrupole coils; therefore an elliptical yoke represents an ideal solution.

The DQ combined-function magnet produces peak fields in the warm bore of 4.3 T and peak fields in the windings of 5.4 T. These fields are comparable to those achieved in large-bore magnets produced 20 years ago for MHD research, particle spectroscopy, and coal sulphur separation. However, the stored energy of the DQ is somewhat less (even though the field volumes are comparable) due to the superposed quadrupole field.

The combined fields also produce a very asymmetric field and force distribution. The fields add on the bottom of the magnet and subtract on the top, so the fields across the bore range from $\simeq 0$ to 5 T. Similarly the fields in the windings are highest where the fields add, giving 5.4 T winding fields and nearly -2 T where they subtract. There is thus a net force between the yoke and coil that must be dealt with due to the asymmetry. The peak linear force densities are 40,000 pounds per inch for the dipole winding and 11,000 pounds per inch for the dipole winding. These forces add on one side and subtract on the other, yielding peak pressures that range from 4680 psi to 2100 psi. Simple pressure-vessel computations in which we limit the material stress to 20KSI yield a 6.0 in thickness for the cold mass force collar. Due to the large radial thickness (3.5 in) of the windings and cryostat (11.8 in) the required 6 in pressure shell is easily accommodated without stressing the coil cold mass. Obviously in a real cold mass the stress will be distributed and the resulting stresses lowered. The large size of the cryostat will allow separate fluid pressure vessels in accordance with the ASME code. This will greatly simplify the final design and result in a much more conservative magnet. A fully clamped winding is planned for the final construction.

DC power for the SHMS magnets is presently designed around low-voltage, high-current commercial power supplies. A DC current of 5000 A at 10 V would be a reasonable choice for SHMS due to the relatively low inductance (0.72 H) and provide easily for a charge time under 30 minutes. The large cold mass and moderate current density ensure that sufficient material is available to absorb a large fraction of the stored energy at a low final temperature during a quench discharge, resulting in a safer overall magnet.

The main characteristics of the superconducting quadrupoles are listed in Table 31. These magnets are identical to the Q1 quadrupole in use as part of the HMS spectrometer in Hall C.

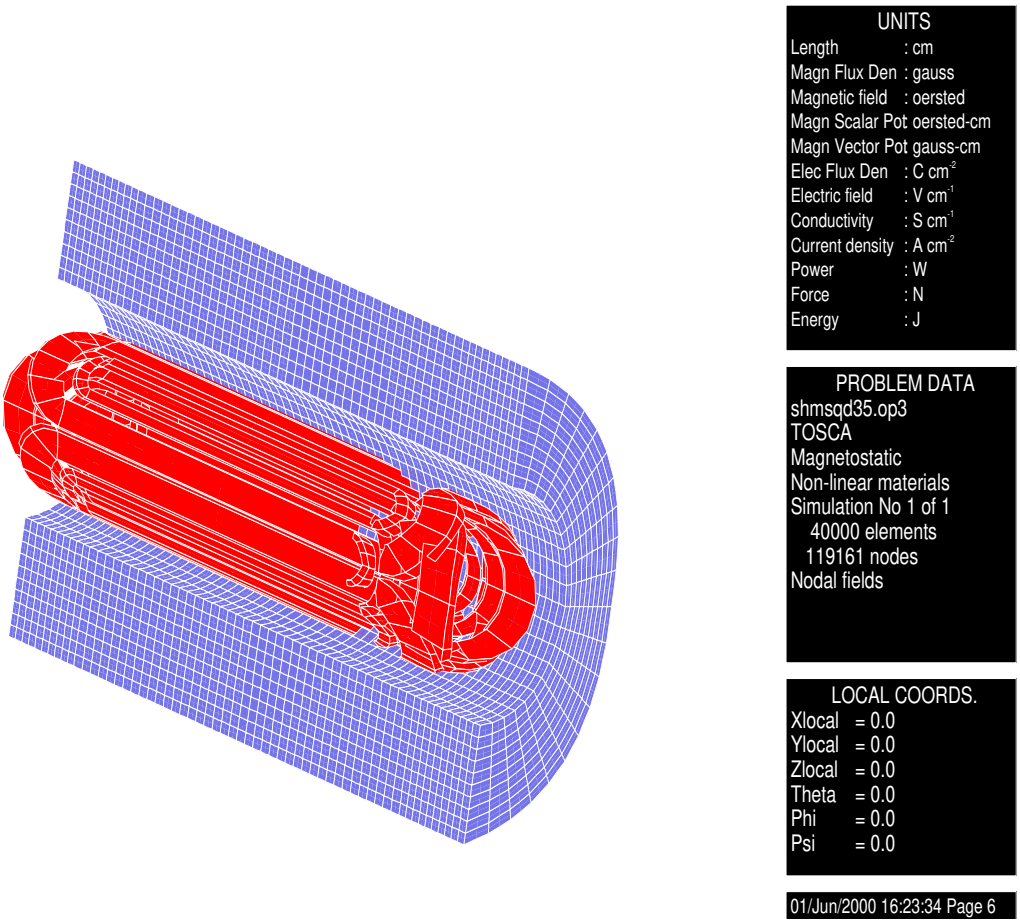

Figure 87: Cutaway view of the combined-function SHMS dipole.

Table 30: Basic parameters of the combined-function dipole for the SHMS.

Overall length	5 m
Warm bore radius	30 cm
Stored energy	11 MJ
Dipole:	
Configuration	4-sector $\cos(\theta)$ superconducting
$\int B \cdot dl$	11.9 T-m
Effective Length	3.45 m
$B(0,0,0)$	3.446 T
Field uniformity dB/B	1×10^{-3} inside 30 cm
Current density	11,000 A/cm^2
Peak force on coil	40,000 lbs/in
Peak pressure	3390 psi
Quadrupole:	
configuration	2-sector $\cos(2\theta)$ superconducting
Gradient (G) (0,25,0)	3.337 T/m
$\int G \cdot dl$	10.99 (T/m)m
Effective length	3.29 m
Gradient uniformity dG/G	1×10^{-3} at 30 cm
Current density	4000 A/cm^2
Peak force on coil	11,000 lbs/in
Peak pressure	1290 psi

Table 31: Main characteristics of the SHMS superconducting quadrupoles.

Effective length	1.89 m
Maximum gradient	8.4 T/m
Warm bore diameter	40 cm
Current at max. grad.	1200 A
Higher-order multipoles	$< 1\%$ at 1000 A
Overall length	2.5 m

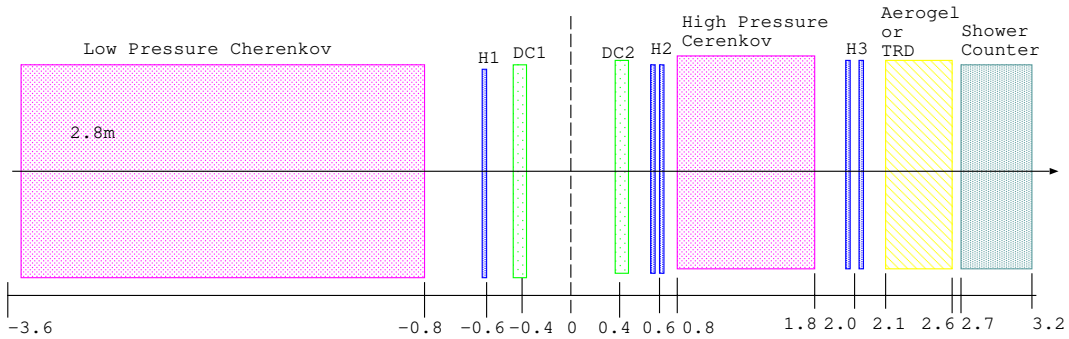

Figure 88: The detector stack of the SHMS. Dimensions along the bottom axis are in meters.

4.D.4 Detectors

The key characteristic of the SHMS detector stack will be flexibility. While the wire chambers, scintillator hodoscopes, and lead glass calorimeter would be more or less permanent fixtures, other detectors may be swapped in and out as experiments require (in some cases remotely). Figure 88 shows a typical SHMS detector stack. Detectors will be designed so as to accept 100% of the beam envelope in the detector stack for a $\pm 10\%$ momentum bite and extended target. The SHMS acceptance will therefore be defined by a limited number of upstream apertures (all easy to measure and survey) facilitating accurate cross-section measurements. The modest size of the SHMS beam envelope at several key points in the detector stack is shown in Fig. 89.

The design of a flexible 11 GeV/c detector stack is fundamentally different than that of the original HMS-SOS detector stacks. First of all, above roughly 3 GeV/c, it becomes very difficult to distinguish hadrons by time of flight over a several-meter baseline even with excellent (*e.g.*, 100 ps) time resolution. This means that one is increasingly reliant upon other technologies such as threshold Čerenkovs. Second, when one designs an experiment it becomes clear that, if threshold Čerenkovs are to be used, then greater flexibility is needed in adjusting the beta threshold. Finally, a gas Čerenkov for electron-pion discrimination at 7.5 GeV/c or above needs to be 2–3 m long to have adequate photoelectron number, so space must be reserved for this, or other technologies must be pursued.

The SHMS detector elements and the collaborating institutions that have expressed an interest in participating in their design, construction, installation, and testing are listed in Table 32.

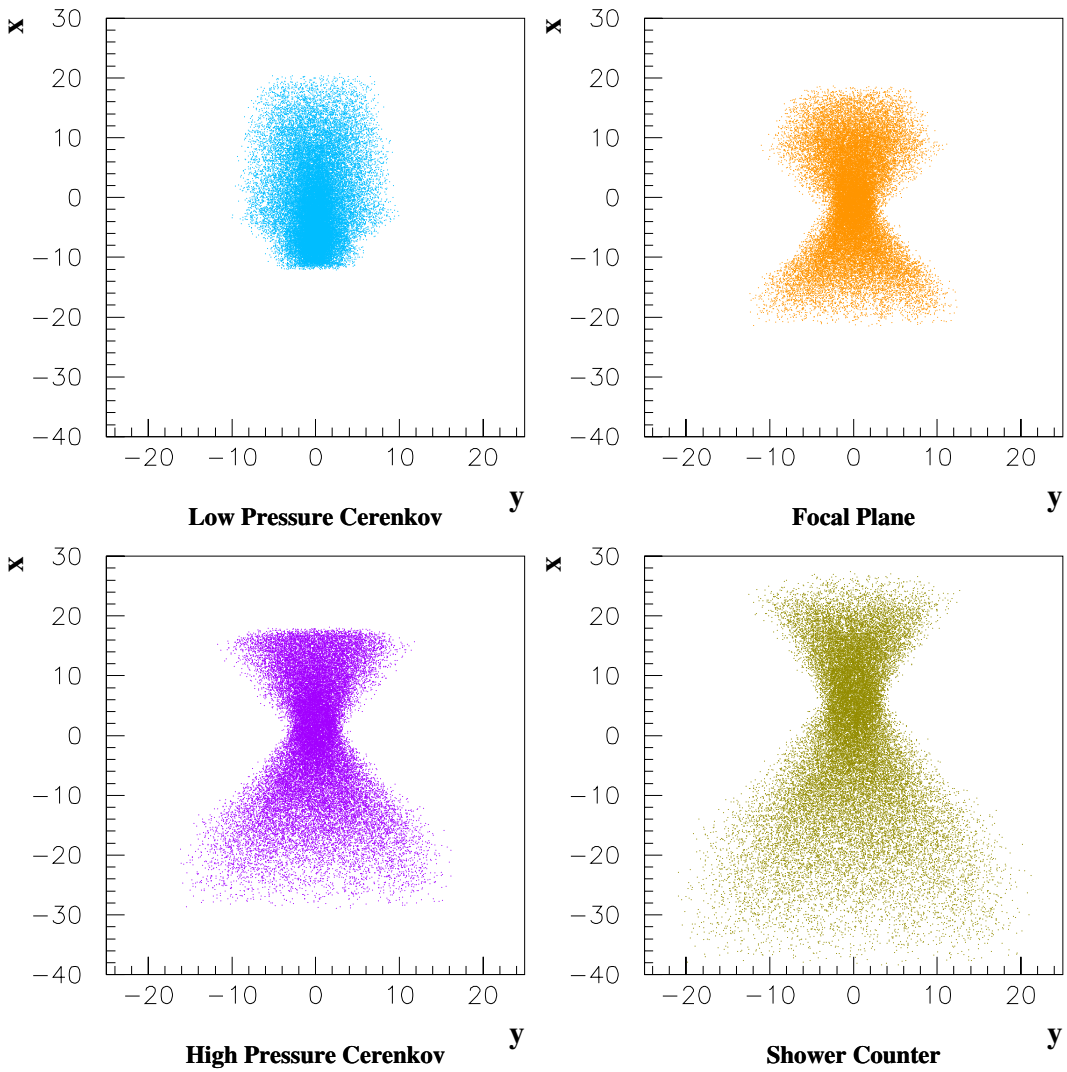

Figure 89: Beam envelope in the detector stack at 2.5 GeV/c for the full momentum bite and full $Y_{\rm tar}$ acceptance at the middle of the low-pressure gas Čerenkov ($z = -2.3$ m), the focal plane ($z = 0$ m), the high-pressure gas Čerenkov ($z = +1.3$ m), and the shower counter ($z = +2.95$ m).

Table 32: The following institutions have expressed interest in writing specifications for the SHMS detectors. These study groups may evolve into design, construction, installation, and commissioning teams. Additional user support or new suggestions for the detector stack are encouraged.

Detector	Institution
Wire chambers	Jefferson Lab
Scint. hodoscope	Jefferson Lab
Calorimeter	Yerevan
Low-pressure Čerenkov	Yerevan
High-pressure Čerenkov	U. Regina
Aerogel	Hampton U.
TRD	Mississippi State U.

Tracking and basic trigger

Particle tracking will be done with a pair of drift chambers, each with six planes of position measurements. The resolution goal would be 100 μm (rms) as in the present HMS wire chambers. The scintillator telescope trigger will be similar to that now used in the HMS, namely a threefold coincidence of four separated planes of scintillator hodoscopes (S1X, S1Y, S2X, and S2Y). These planes will contain 8-cm-wide, overlapping scintillator elements of 1 cm thickness. Although in principle capable of yielding 50 ps (rms) focal plane timing resolution, we have found that such a system is realistically limited to 100 ps (rms) focal plane timing resolution without heroic measurement to correct for TDC drifts. As demonstrated in the present HMS-SOS setup, this will still provide more than 10-sigma separation of real and random coincidence peaks.

Particle identification

Electron-hadron discrimination A lead glass shower counter will provide a tag for electrons. This would normally be augmented by a gas Čerenkov when electron-pion discrimination is needed. Below roughly 6 GeV/c, the shorter (so-called high-pressure) gas Čerenkov downstream of the wire chambers would be used. At higher momenta, a gas Čerenkov would have to operate well below atmospheric pressure. This means that the device would require an active length of 2–3 m (several times longer than the existing HMS gas Čerenkov) to achieve a reasonable photoelectron yield. Due to limited space in the detector hut, this low-pressure (LP) gas Čerenkov must be located upstream of the drift chambers. Simulations demonstrate that the resolutions at 7.5 GeV/c using the LP gas Čerenkov (filled with 1/3 atm C4F10) are comparable to or better than those

obtained at 2.5 GeV/c with the LP gas Čerenkov under vacuum as in Fig. 86.

Distinguishing species of hadrons Experiments which detect pions will make use of a high-pressure (HP) gas Čerenkov employing C4F10. This gas has been used successfully for years in the HMS gas Čerenkov for electron and pion detection at pressures of 0.5–1 atm. In reality the HP gas Čerenkov device would have variable pressure with a nominal operating range of 0.5–2 atm, which would typically be adjusted remotely except when the windows needed to be changed.

Experiments where kaons are detected will generally benefit from an aerogel detector. Covering a large momentum range will require aerogels with indices ranging from 1.01-1.06. We have reserved sufficient room such that two or three aerogel counters could be used simultaneously in the detector stack.

Other detector technologies Transition radiation occurs when a charged particle crossing a dielectric boundary is ultrarelativistic [Gi46]. The number of transition radiation photons is increased by increasing the number of boundary crossings. Due to interference effects created by the periodic arrangements of the boundaries, only charged particles with a Lorentz factor $\gamma >$ 1000 produce transition radiation [Ar75]. At JLab Upgrade energies this means that a transition radiation detector (TRD) could be used to distinguish between electrons and more massive particles. One nice feature of transition radiation is that the energy of the radiation increases with γ and is not proportional to its velocity, β. This makes TRD's increasingly useful at high energies (in contrast to time-of-flight techniques or gas Čerenkov detectors, whose length must increase as the square of the momentum for an equivalent number of photoelectrons). The transition radiation photons are emitted in the X-ray range; hence the radiator needs to be made of low-Z material. Typically, a TRD will consist of multiple modules, where a module contains a radiator followed by a proportional chamber filled with xenon to detect the photons.

A TRD is well suited for the SHMS – a 50-cm-long detector should produce a pion rejection factor of 200–300 at 90% electron efficiency. The C TRD would utilize cluster-counting particle identification. This particle ID method has an advantage over a total-charge method since the distribution of the number of ionization clusters is better behaved than the total ionization energy.

We are also considering the use of a ring-imaging Čerenkov counter (RICH) combining both gas and aerogel radiators as employed by HERMES. While interesting in that it could provide definite signatures for multiple particle species through measurement of the Čerenkov angle (unlike a threshold Čerenkov), much more study is needed. Such a device would be most useful if fast

PID-trigger information could be obtained (*e.g.*, kaons only) and the RICH counter covered a very broad range of momentum.

4.E Hall D

4.E.1 Introduction

The purpose of the Hall D experiment is to search for so-called gluonic mesons with masses up to $2.5\,\mathrm{GeV/c^2}$. The identification of such states requires knowledge of their production mechanism, the identification of their quantum numbers, J^{PC}, and measuring their decay modes. These in turn require a partial wave analysis of exclusive final states. The decay products of produced mesons must be identified and measured with good resolution and with full acceptance in decay angles. In many cases, the decays of mesons involve a chain of particle decays. The Hall D detector must therefore be hermetic with an effective 4π coverage with the capability of measuring directions and energies of neutral particles (γ, π^0, η) and momenta of charged particles with good resolution. Particle identification is also required.

The partial wave analysis technique also depends on high statistics and, in the case of incident photons, also requires linear polarization. As discussed in Section 2A, the latter is needed to identify the production mechanism. The linear polarization is achieved by the coherent bremsstrahlung technique. The degree of linear polarization and flux of photons in the coherent peak fall dramatically as the photon energy approaches the endpoint energy. On the other hand, it is desirable to have photon energies high enough to produce the required masses with sufficient cross section and with sufficient forward-boost for good acceptance. For a fixed incident momentum and a fixed resonance mass, it is also desirable to have a fairly constant $\mid t \mid_{\mathrm{min}}$ over the natural width of the resonance. This also requires sufficiently high incident photon energy. An operating photon energy between 8.0 and 9.0 GeV produced from a 12.0 GeV electron beam represents an optimization of beam flux, cross section, and degree of polarization. The Hall D detector is optimized for this energy range. Extensive Monte Carlo simulation has been performed to optimize the detector's ability to reconstruct exclusive final states. Acceptances are nearly 90% for many complicated channels, and the detector resolutions have been balanced to facilitate excellent reconstruction of the events, and allow kinematic fitting to reduce background contamination of events, thereby facilitating the partial wave analysis.

4.E.2 The Photon Beam and Polarization

Linearly polarized photons can be produced in the desired energy range by using the technique of coherent bremsstrahlung. A horizontal plan view of the photon beam line is shown in Fig. 90 with the major components labeled. The electron beam enters the figure from below ground at the left

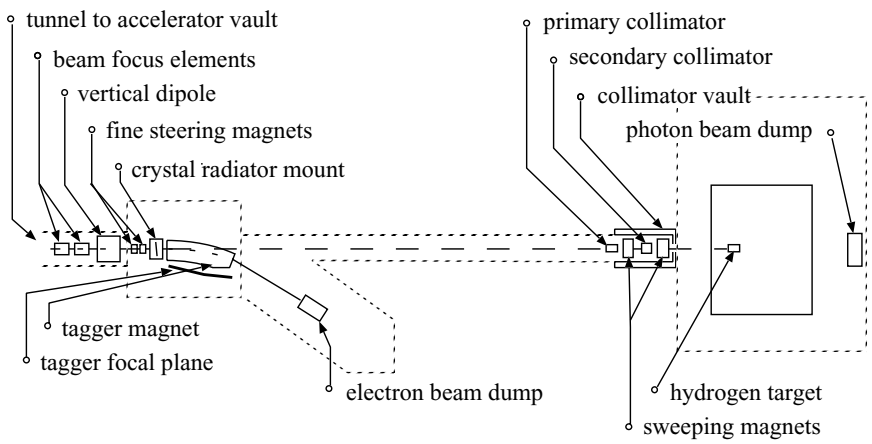

Figure 90: A schematic plan view of Hall D photon beam line, shown in the horizontal plane as viewed from above. The objects in this figure are not drawn to scale.

and is bent into the horizontal plane to enter the tagger building. There it passes through two small dipoles to impinge upon the bremsstrahlung radiator.

The photon tagger and beam collimation

After its exit from the radiator, the electron beam passes into the tagger magnet where the primary beam is bent in the direction of the electron beam dump. The radiator crystal is thin enough that most of the electrons lose less energy in traversing the radiator than the intrinsic energy spread of the incident beam. Those electrons which lose a significant fraction of their initial energy inside the radiator do so by emitting a single bremsstrahlung photon. These degraded electrons are bent out of the primary beam inside the tagger magnet and exit the vacuum through a thin window, passing through air for a short distance to strike the focal plane of the spectrometer. The primary electron beam is contained inside vacuum all the way to the dump.

The Hall D tagging system will consist of a dipole magnet spectrometer with a set of plastic scintillation counters in the focal plane to tag photon energies between 50% and 95% of the incident electron energy. The tagging spectrometer magnet envisioned for Hall D is modeled closely on the existing tagger magnet in Hall B. Although the Hall D tagger will operate at a much higher energy, the combination of smaller deflection angle and smaller dynamic range (50% to 95% of the incident energy instead of 20% to 95%) results in a device which is comparable to the Hall B tagger in most of its dimensions, allowing the use of existing solutions to many engineering problems.

Such a tagging system will allow us to measure the photon energy to an accuracy of 0.1%, a limit which is set by detector constraints on reconstructing missing masses. The collaboration is also investigating a sliding tagger counter. This would facilitate diagnostics and calibration including the measurement of the crystal angle. It could also reduce the electronics costs associated with the tagger readout.

The photons that are produced in the radiator pass through a small hole bored in the return yoke of the tagger magnet to exit the vacuum through a thin window in the forward direction. They then pass into a transfer pipe, which may either be evacuated or filled with helium to reduce photon beam degradation due to interactions, and travel to the experimental hall. Just before entering the hall the photon beam passes through a system of collimators and sweeping magnets. In the figure they are shown in a separate enclosure for shielding purposes. The primary collimator defines the part of the photon beam that is allowed to reach the target. Debris from interactions along the inside surface of the collimator bore forms a halo around the photon beam that exits the collimator. The charged component of the halo is deflected away from the beam axis by a dipole "sweeping" magnet just downstream of the collimator. A secondary collimator follows the sweeping magnet to stop the deflected shower particles and block the halo of secondary photons generated by the first collimator. The secondary collimator is of a larger diameter than the primary and so sees a reduced rate of secondary interactions on the inner surface of the hole. What new showers are generated there are cleaned up by a second sweeping magnet. The beam then passes through a final collimating aperture into the experimental hall. This triple-collimation system was copied from the setup developed at SLAC [Ka75].

The collimated photon beam, now only a few millimeters in diameter, is delivered to the experimental target. After passing through of order 3% radiation lengths of target, the photon beam passes through the detector and into the photon beam dump at the back of the hall. Based upon a design upper limit of 60 kW (5 μA at 12 GeV) being delivered to the electron beam dump, the total power in the photon beam is at most 1.5 W in the experimental hall and at most 15 W in the collimator enclosure. The safety issues of such a beam have been reviewed by Jefferson Lab's RadCon group. As an additional safety constraint, permanent magnets are being installed in the photon beam downstream from the tagger building to prevent an accidental loss of the electron beam into Hall D. These magnets have been obtained as surplus from FermiLab.

The effects of collimation and the thickness of the radiator are demonstrated in the calculated spectra shown in Figs. 91 and 92. First, note that the collimation angles are very small, which requires a long flight path of 80 m in order that the collimator can be larger than the intrinsic beam spot size; otherwise the collimator is cutting in transverse coordinate instead of in angle.

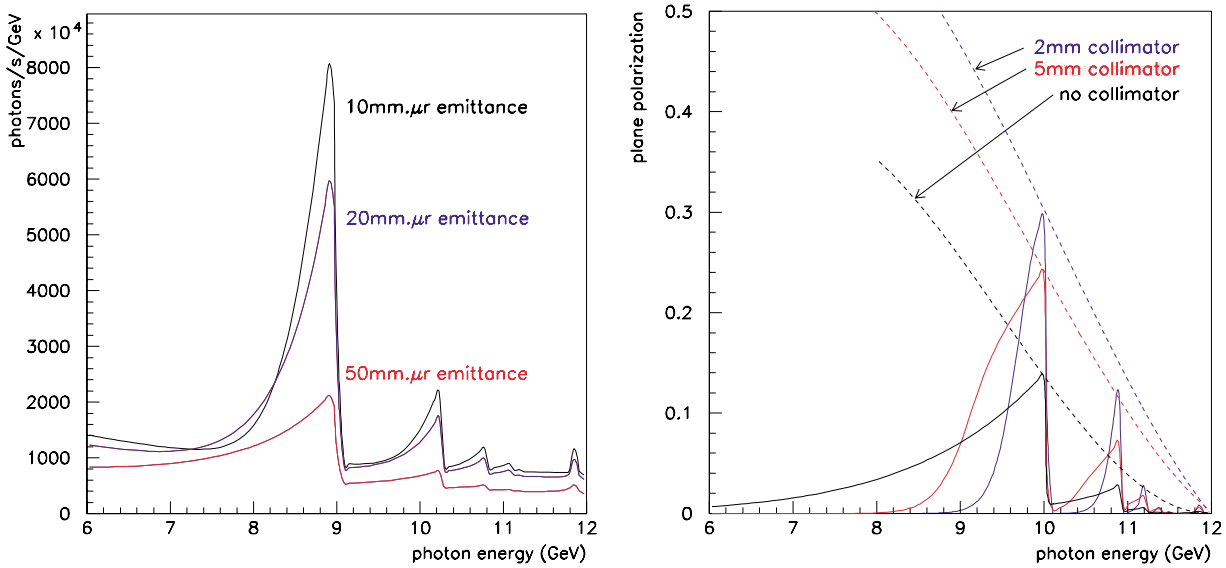

Figure 91: Left: The effect of collimation on the coherent bremsstrahlung spectrum (various collimation diameters are given). Right: Plane polarization of the coherent bremsstrahlung.

This distance is, in fact, a sensitive function of the electron beam emittance from the machine, and must be increased in inverse proportion to the beam emittance if the effectiveness of collimation is to be maintained.

Polarization via coherent bremsstrahlung

The net polarization of the beam under different collimation conditions is shown in Fig. 91. The dashed curves show how the maximum polarization in the peak varies as the peak energy is changed by rotating the crystal. The polarization in all cases is zero at the endpoint. Without collimation it rises as $(k-E)^2$, one power coming from the intensity of the coherent peak relative to the incoherent component going to zero linearly at the endpoint, and the other from the intrinsic polarization of the coherent photons also behaving like $(k-E)$ near the endpoint. Collimation allows one to essentially isolate the coherent component, so that the polarization available to the experiment rises from zero at the endpoint in a linear fashion. The dashed curves in Fig. 91 demonstrate this point.

In order to obtain the full polarization enhancement from collimation, it is necessary to have a distance between the radiator and collimator of about 80 m. This distance scale is set by the requirement that the collimator aperture must be large compared to the size the electron beam

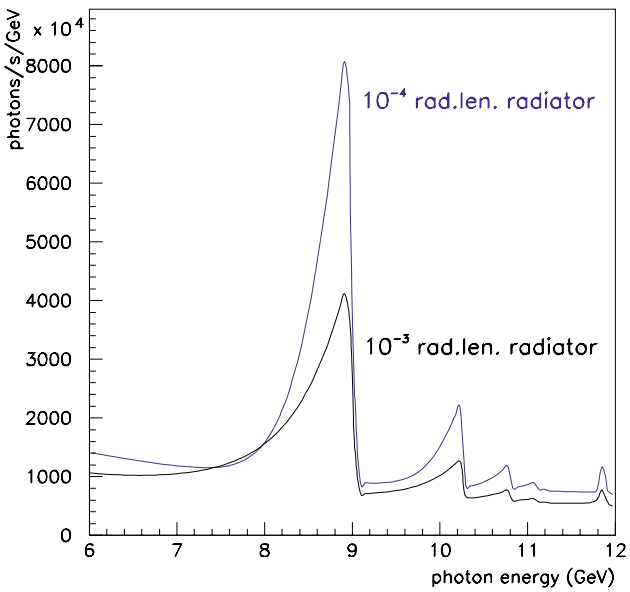

Figure 92: The collimated coherent bremsstrahlung spectrum for two crystal radiator thicknesses.

spot would be on the collimator, but small compared to the actual photon spot size. Fig. 91 shows the maximum polarization as a function of radiator-collimator distance for a coherent peak at 9 GeV. The collimator diameter is adjusted in this calculation to keep the collimation half-angle at $0.5\,m_e/E$. At zero distance the collimator has no effect except to attenuate the beam, and so the uncollimated polarization from coherent bremsstrahlung is obtained. At 100 m separation distance the polarization enhancement has saturated. The design for Hall D calls for a radiator-collimator distance of 80 m.

The thicknesses of the crystal radiator is limited by multiple scattering of the electron beam as it passes through the radiator, which causes the divergence of the incident beam to grow, thereby enlarging the photon beam spot on the collimator face and degrading the degree to which collimation discriminates against the incoherent component in favor of the coherent part. It is bounded from below by the fact that the crystal must be of some minimum thickness in order to achieve the full coherent gain. For a 12 GeV beam energy and a 6 GeV coherent photon the coherence length is 18 nm. The coherence length does not impose a practical limit on how thin the radiator should be. The effects of multiple scattering are best presented by showing the calculated spectra for various radiator thicknesses. In Fig. 92 is shown the photon spectrum for a 20 μm (10^{-4}) and a 100 μm (10^{-3}) radiator to demonstrate the effect. The 100 μm spectrum is scaled down by a factor of 5 to facilitate the comparison, but it is clear that for a significant coherent gain, the crystal thickness must be near 20 μm.

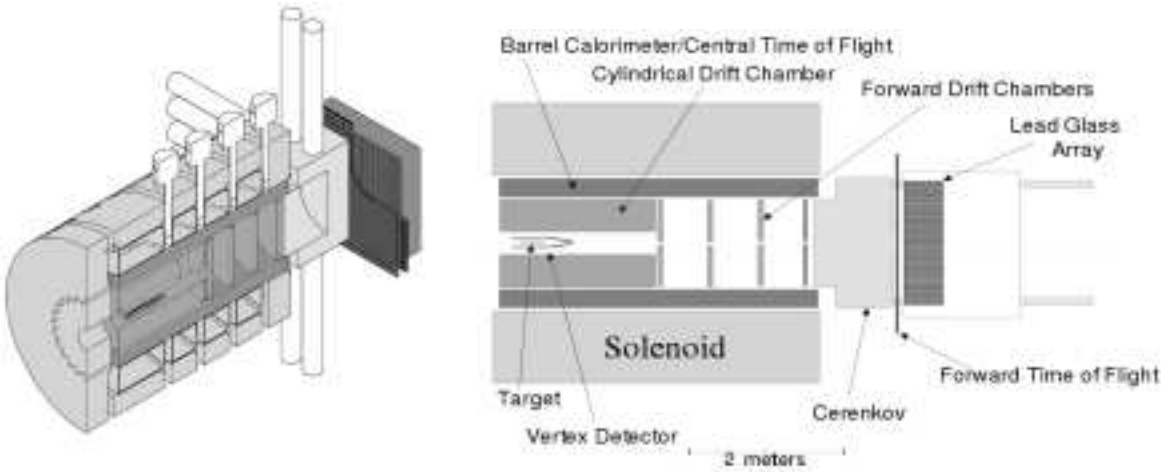

Figure 93: A 3D cut-away view of the Hall D detector (left) and schematic diagram of its major subsystems (right).

A committee chaired by David Cassel (Cornell) and consisting of Frank Close (Rutherford Laboratory), John Domingo (Jefferson Lab), William Dunwoodie (SLAC), Donald Geesaman (Argonne), David Hitlin (Caltech), Martin Olsson (Wisconsin), and Glenn Young (Oak Ridge) reviewed the project plans in December 1999 [Ca00]. The Cassel committee identified the availability of thin diamond crystals as one of the critical R&D areas for Hall D. Should it prove impossible to achieve the proposed level of linear polarization, the committee believed, it will be necessary for the collaboration to make the appropriate modifications to the proposed physics program. In response to this concern, *Hall D collaborators have obtained diamond wafers that are sufficiently thin for Hall D purposes; these wafers will be tested at Mainz in 2001.*

4.E.3 The Hall D Detector

The Hall D detector has been optimized to provide nearly hermetic acceptance for both charged particles and photons. In addition, a combination of particle identification systems will allow very good K-π separation. Optimization will allow the detector to fully reconstruct exclusive many-body final states. In conjunction with high statistics, this will allow us to do excellent partial wave analyses of many final states. Figure 93 is a schematic representation of the proposed detector; the individual subsystems are discussed in more detail below. A more detailed description can be found in the Hall D Design Report [HD99].

The superconducting solenoid

Momentum analysis of charged particles will be achieved using a superconducting solenoid and tracking chambers. The superconducting solenoid already exists. It was built for the LASS detector at SLAC and later moved to LANL where it was used for the MEGA experiment. The magnet is described in a technical note [As87]. The solenoid magnet provides a 22.4 kG magnetic field parallel to the beam direction. The inside diameter of the magnet is 185 cm and its overall length is 465 cm. The fiducial region within the bore is 320 cm in length and 75 cm in radius. Within this region the field homogeneity is better than $\pm 3.1\%$. Along the beam axis the homogeneity improves to $\pm 0.9\%$.

The Cassel committee [Ca00] identified that the R&D area of greatest concern was to ensure that the magnet is still functional, particularly the fourth coil, which has not been used for at least 15 years. *In March 2000, an assessment team went to Los Alamos to check the magnet. The team found that all coils appeared to be in working order and estimated that the magnet had at least another 25 years of life* [ML00].

Moving and refurbishing costs of the magnet are estimated at about \$1M, while replacement costs are estimated to be \$12M. Negotiations between Jefferson Lab and LANL are underway to have the magnet transfered to JLab.

Particle tracking and particle identification

The system of tracking chambers in the Hall D detector must cover as close to an effective 4π solid angle as possible over a wide range of particle momenta and have sufficient momentum resolution to be able to identify missing particles. In the solenoid region, the chambers are inside the barrel calorimeter. The location of the target very near the entrance to the solenoid, coupled with the energies involved which force the reaction products into forward angles, result in an effective 4π coverage, even though the geometrical coverage around the target is less than that. The chambers also must extend as close to the beam line as possible. Near the target, this will provide very accurate vertex information which will be important in identifying decaying particles (*e.g.*, K_S, Λ, Σ, ...). In the forward region, this is needed to reconstruct very fast small-angle particles (down to nearly 0°). Finally, it is necessary that near the target, the tracking be able to separate π's and K's up to momenta of about 0.5 GeV/c – a regime where dE/dx measurements will work. To satisfy the tracking requirements a starting point based on the LASS detector [As87] was taken. A series of three different tracking elements is taken, with each element optimized for a particular region in the detector as shown in Fig. 93.

The vertex system (VTX) surrounds the target, and detects outgoing particles at angles from 1° to 90° for the full length of the target. The VTX has several purposes. First it will be used to provide accurate tracking information very close to the target. These track elements must be sufficiently well defined to be connected to the other tracking chambers. Second, the VTX must provide a fast signal which can be used in the level 1 trigger of the experiment, in particular a start signal for the event. Finally, it is a critical element of all time-of-flight systems. The vertex detector will consist of two detector packages. One will be optimized for timing purposes, and the other will provide fast tracking information. (See Fig. 94.)

The timing detector will consist of a cylindrical array of ten scintillator paddles. This will allow us to cover scattering angles between 1° and 90° for the full length of the target. The scintillators have a thickness of 5 mm, which reduces to 2 mm in the forward direction. This will provide a good light output and therefore a good timing signal. Using Bicron BC-404 scintillating material in combination with fast photomultipliers, we expect to achieve better than 120 ps overall timing resolution. The collaboration is investigating the trade-off between material thickness and time resolution.

The fast tracking detector will consist of three super-layers of fibers, each containing two layers to minimize dead space. The central layer will be arranged around the target and parallel to the beam. It will determine the azimuthal angle. The z position is deduced from the two outer layers. They will be wound in two opposite helices around the first layer. In order to function in the high magnetic field, we are studying the possibility of using visible light photon counters (VLPC) developed by Rockwell in collaboration with Fermilab [Pe89]. The spectral sensitivity of the VLPC's requires us to use SCSF-3HF multi-clad scintillating fibers from Kuraray which are also the least susceptible to radiation damage. One of the main advantages of using VLPC's is their large quantum efficiency of approximately 80% [Wa97] for the light produced by the fibers together with a very high rate capability of 10^8 single photoelectrons per second. The design of this detector system will closely follow the prototype system developed [Ba96] by the D0 collaboration at FNAL. The expected position resolution will be at least 1 mm.

The cylindrical drift chamber (CDC) surrounds the VTX and provides very good $r-\phi$ information and moderate to good z information. This chamber also provides dE/dx information for tracks which do not reach any time-of-flight detectors. The CDC is used to accurately track particles between polar angles of 20° back to 170°. To minimize material in the forward end plate of the chamber, one would like a self-supporting chamber. This leads to a straw chamber, where the straw walls support much of the wire tension. The disadvantage of this design is the difficulty

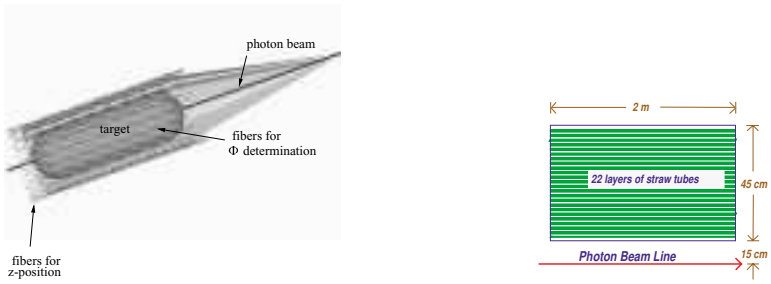

Figure 94: The start counter/vertex chamber (left) and the straw tube chamber (right).

of making dE/dx measurements in a circular straw tube. The planned design has the chamber filled with 5200 1-cm-diameter straw tubes arranged in 22 layers. The tubes are assumed to have an $r - \phi$ resolution of 200 μm, while resolution along the wire length will be obtained by placing about half of the layers at a 6° stereo angle. A typical hydrocarbon drift gas will have v_d on the order of 5 cm/μs, meaning maximum drift times will be on order of 100 ns.

The forward drift chambers (FDC) are disk-shaped drift chambers. The basic drift package is a plane of wires with 150 μm spatial resolution between two planes of cathode strips. The strips are arranged in a u and v geometry with respect to the wires, allowing the reconstruction of a 3-D space point from each hit. The chambers are arranged in packages of six to provide a small track segment to facilitate later linking of tracks. Given the number of spiraling tracks, it is critical that these chamber packages not only provide good spatial resolution, but also reasonable direction information. The basic chamber element is a disk of outer radius 60.0 cm, the wires strung as chords across the chamber. With a 1.0 cm wire spacing, each chamber will contain 119 wires. In addition, there will be an equal number of cathode strips on each face. These are arranged in a u–v pattern with respect to the wires. The wires that cross through the beam line will be deadened out to a radius of about 3.5 cm by placing material such as styrofoam in the chambers.

Monte Carlo studies show that the combined tracking system provides very good momentum resolution for the event topologies in Hall D. The system is sufficient to identify undetected particles by missing-mass cuts. In particular, a missing neutron can be separated from a completely missing recoil Δ for most kinematic regions. Detailed information on resolutions can be found in Ref. [HD99].

Electromagnetic calorimetry (EM) in the barrel region of the Hall D detector covers the approximate polar angular range $14^\circ < \theta < 138^\circ$ (indicated as barrel calorimeter in Fig. 95). The goal of the calorimetry is to detect and measure photons from the decays of π°'s and η's, which, in turn, can come from the decays of produced mesons, or from an excited baryon (N^* or Δ). The positions and energies of the photons must be of sufficient accuracy to allow for a complete kinematic reconstruction of the event. Finally, for events with only charged particles, it is essential to be able to veto on neutral missing energy. Hence, nearly hermetic coverage is critical. For selected triggers, neutral energy requirements (or vetoes) are relatively easy to implement.

The barrel calorimeter, shown schematically in Fig. 95, will utilize scintillating fibers embedded in a lead (or possibly tungsten) matrix to make a relatively high-resolution sampling calorimeter. Advantages include speed, cost, ease of readout, and the fact that it is based on a proven technology. This technology has been used in calorimeter design and operation for more than a decade. The ratio of the active scintillator to the passive high-Z material, as well as the diameter of the fibers, can be tuned to enhance resolution, to determine the radiation length, and to achieve uniformity in the electromagnetic to hadronic response (the e/h ratio). For high-resolution EM performance, the Jetset detector developed at Illinois [He90] was the first designed specifically to optimize EM resolution. The recipe produced a detector comparable to lead glass at a considerably lower cost and with approximately half the radiation length. Our design for Hall D follows this concept but would be a full 12.5–15 X_0 thick at normal incidence and considerably longer. Realization of these changes fortunately can be based on the KLOE calorimeter at DAΦNE, where they have been building a device of this length with an even larger inner diameter [An96]. They have achieved an excellent energy resolution parameterization of $\sigma/E \approx 4.4\%/\sqrt{E}$ in a half-length prototype.

An important feature of these detectors is the signal rise-time and overall duration. Because fast plastic scintillator is used, integrated signal time can be kept below 100 ns with shorter times possible if deemed necessary for rate considerations. At the expected maximum luminosity, no problems are anticipated. With rise-times of a few nanoseconds, excellent timing can be expected for each of the PMTs involved in collecting the light from a shower. Time differences from the two ends produce the z coordinate of the hit. The mean time of the two readout ends can be used

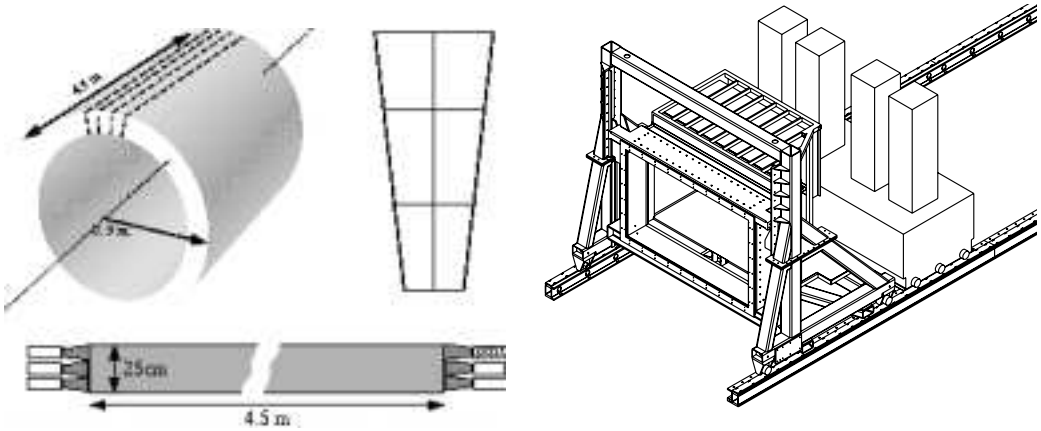

Figure 95: Left: Schematic diagrams of the barrel calorimeter. The 4.5-m-long elements will be stacked in wedges. Right: A sketch of the Pb-glass array as modified for the Hall D detector. The glass will be stacked in a circular arrangement to match the solenoidal geometry.

to determine the particle time of flight (TOF). TOF coupled with the track length and momentum then yields particle mass. In the KLOE design, timing of $\approx$ 250 ps (rms) was achieved, and improvements are possible.

A circular lead glass array will serve as the forward electromagnetic calorimeter for the Hall D detector. The Brookhaven National Laboratory E852 lead glass calorimeter [Cr98], (LGD), will be salvaged and, with minor modifications, will be configured for Hall D use.

Operating an electromagnetic calorimeter, like the LGD, near a photon beam line could be a concern given the backgrounds one might expect with a tagged bremsstrahlung photon beam. For this reason, the experience with the LGD used in the Radphi experiment in the Hall B photon beam is of particular relevance. Because of the high quality of the photon beam, beam-associated backgrounds were manageable, even when operating at an endpoint energy of 4 GeV. At higher energies the beam spot size will be even smaller, and the LGD energy resolution will improve.

Charged particle identification (PID) separates $\pi^{\pm}$ from $K^{\pm}$ from p (and the occasional $\bar{p}$). (We do not consider $e^{\pm}$ nor $\mu^{\pm}$ identification explicitly, but they can be separated from hadrons at some level using the electromagnetic calorimeters.) Two detector systems will be constructed explicitly for this purpose, namely the time-of-flight hodoscope and the Čerenkov detector. Both of these address PID in the forward region, where velocities are close to c, and the separation is most difficult. In the solenoid, we expect to make use of dE/dx in the drift chambers and timing in the barrel calorimeter. Furthermore, constrained fitting is a generally useful tool for identifying

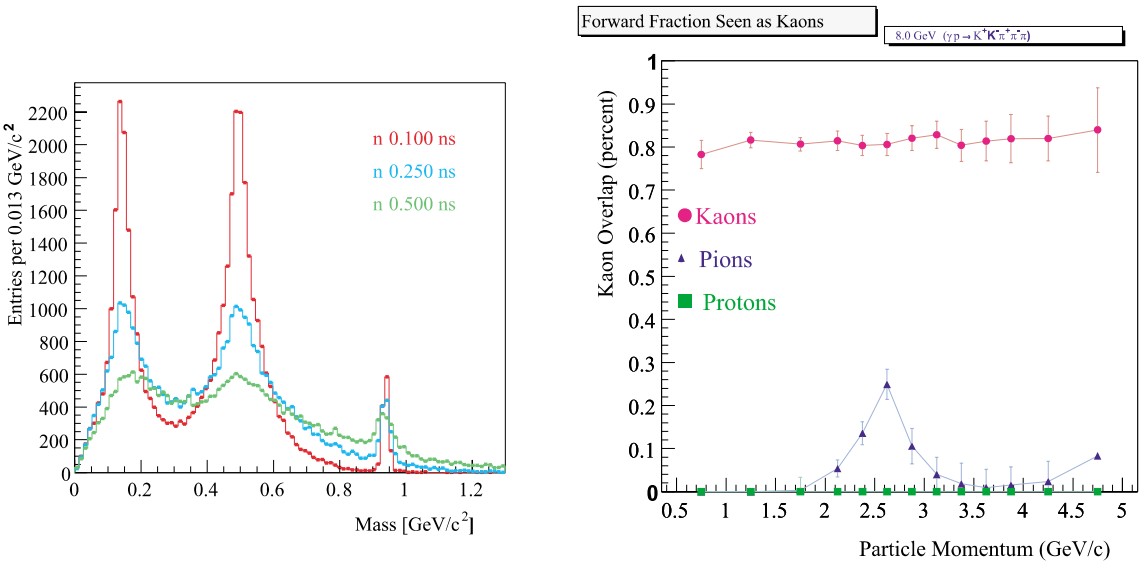

Figure 96: Left: Particle mass as reconstructed from the particle momentum and the time of flight for several timing resolutions. Right: K-π-p separation for individual tracks in the Hall D detector, (timing resolution of 100 ps is used).

the event topology as a whole.

If the particle momentum is not too high, time of flight is useful for PID in the forward region. For TOF scintillators that are $\approx$ 2 m long, rms time resolutions on the order of 100–120 ps are typically achievable using well-established techniques [Mo79, Be82]. With improvements in photomultiplier design, however, one can achieve 50 ps rms for detectors with long, narrow geometry. Superior time resolution has also been achieved with mesh PMTs which will work well in a high magnetic field. In Fig. 96 is shown the reconstructed particle mass from time of flight and charged tracking for several different time resolutions. Hall D is aiming for timing resolutions in the forward direction of about 100 ps, which when combined with the start counter would yield an overall resolution of about 150 ps. Beam tests of prototype designs are bing carried out in collaboration with the group at Protvino; early results indicate we are well on the way to achieving the needed time resolution.

The Čerenkov detector is planned to be a gas-filled threshold detector running at atmospheric pressure. It will be used to identify high-energy pions when TOF measurements cannot distinguish between pions and kaons. Current studies suggest that a C_4F_{10}-filled Čerenkov detector ($n = 1.0014$) will be a good match to the kinematics of Hall D reactions. For individual tracks, the

results of the Čerenkov detector coupled with the time-of-flight system are shown in Fig. 96.

Because the Hall D experiment will be reconstructing exclusive final states, perfect K-π separation for all tracks is not necessary. Detailed Monte Carlo studies using the above detectors and imposing additional constraints such as the total strangeness in an event, and kinematic fitting have been performed. We find that combining all available information will make for a very efficient particle identification system for Hall D events.

4.E.4 Rates, Trigger, and Data Acquisition

Table 33 gives the total hadronic rate, and the tagged hadronic rate for fixed electron beam conditions for various energies of the coherent peak. For $E_\gamma = 9\,\mathrm{GeV}$ and $10^8\,\gamma/s$ in the peak, the experiment will have a total hadronic rate of 365 kHz and a tagged hadronic rate of 14 kHz. Initial operating conditions will be at about 10% of these values, ($10^7\,\gamma$/s), but as the trigger improves, and the detector is better understood, rates will be pushed up towards the 10^8 number.

An essential feature of the Hall D design is to build pipelining into the entire trigger, digitizer, and data-acquisition systems at the outset. This has the virtue of allowing us to upgrade from initial photon fluxes of $10^7\,\gamma$/s to eventual fluxes of $10^8\,\gamma$/s. The level 1 trigger makes a decision based on detector elements which measure hadronic multiplicities (track counts) and energies. The start counter and barrel and forward TOF detectors provide the track count while the barrel and forward calorimeters determine the energy. A tight tagger OR/start counter coincidence also is used as input to the level 1 trigger for low photon fluxes of $\approx 10^7\,\gamma$/s. For high photon fluxes ($\approx 10^8\,\gamma$/s), the tagger OR/start counter coincidence is not a useful requirement. It will be necessary to impose a software level 3 trigger which uses input from all detectors.

The data-acquisition goal for Hall D is to accept the level 1 trigger rate without incurring any DAQ system dead-time. The high rate of 70–180 kHz drives the design of the trigger, the front-end electronics, and the DAQ system. When the level 1 trigger is asserted, a time slice of each ring buffer will be copied, compressed, and stored. Events will be buffered into groups of at least ten on each electronics board and then transferred first across a backplane to be built into crate event fragments and then to a computer farm to be built into complete events. The farm will perform a quick analysis to reduce the event rate by approximately a factor of 10 before recording to magnetic media. This design allows Hall D to start running with a modest tagged-photon rate and then to scale up by an order of magnitude.

The goal of the level 3 trigger is to reduce the event rate given by the level 1 trigger to an

Table 33: Operating parameters for an experiment using the coherent bremsstrahlung beam. The calculation assumes a 12 GeV electron beam energy and a 3.4 mm collimator 80 m downstream from a radiator of thickness 10^{-4} radiation lengths. The electron beam current is taken to be 3 μA. The rates in the detector (last two rows) are calculated for a 30 cm hydrogen target and an open hadronic trigger.

E of peak	8 GeV	9 GeV	10 GeV	11 GeV
N_γ in peak	185 M/s	100 M/s	45 M/s	15 M/s
Peak polarization	0.54	0.41	0.27	0.11
(f.w.h.m.)	(1140 MeV)	(900 MeV)	(600 MeV)	(240 MeV)
Peak tagging efficiency	0.55	0.50	0.45	0.29
(f.w.h.m.)	(720 MeV)	(600 MeV)	(420 MeV)	(300 MeV)
Power on collimator	5.3 W	4.7 W	4.2 W	3.8 W
Power on target	810 mW	690 mW	600 mW	540 mW
Total hadronic rate	385 K/s	365 K/s	350 K/s	345 K/s
Tagged hadronic rate	26 K/s	14 K/s	6.3 K/s	2.1 K/s

acceptable on-tape rate. In low-intensity running (10^7 tagged photons/s) the level 1 trigger rate is expected to be 15 kHz. Since the DAQ system is being designed to handle this rate to tape, the level 3 trigger farm will not have to cut any events, although it may be used to reduce the event rate somewhat. In high-intensity mode where the level 1 rate is 70 to 180 kHz, the level 3 trigger must be able to reduce the event rate by a factor of 10.

Most of these unwanted events result from an untagged (mostly lower-energy) photon interacting in coincidence with a tagged photon. Rejecting these events means that level 3 must be able to calculate, with reasonable accuracy, the energy of the photon which produced the event. This involves accurately reconstructing tracks, matching them with the calorimeters, and adding additional energy deposited by neutral particles in the calorimeters.

Because of the accuracy requirements and the demands of linking information from different detectors, we have decided to use a processor farm architecture for level 3 instead of building a dedicated hardware processor. All events passing the level 1 trigger will be read into the level 3 processor farm where they will be reconstructed; events passing the cuts applied will then be written to tape. This approach allows for algorithmic flexibility and improvements, and the ability to cost-effectively adjust to higher rates, but it does put pressure on the DAQ system.

An estimate of the processing power required can be made using the Hall B full event analysis as a model. Hall B has similar-sized events, and their reconstruction time should be quite similar to

Table 34: Rates, sizes, and processing requirements for the level 3 trigger. A 35 SpecInt95 processor corresponds to a PIII 750 MHz machine. Moore's law scaling will lead to 350 SpecInt95 processors by early 2005, and such a box will cost about $2K.

	Low Rate	**High Rate**
Event size	5 kB	5 kB
Event rate to farm	10 kHz	180 kHz
Data rate to farm	50 Mbytes/s	900 Mbytes/s
Link technology	100 megabit Ethernet	Gigabit Ethernet
SpecInt95 for L3	2500	45,000
Num 35 SpecInt95 processors/link	70	1280
Num 350 SpecInt95 processors/link	7	128
Total Num dual 350 SpecInt95 nodes	4	64

Hall D. Currently, Hall B is able to fully reconstruct an event off-line in 100 ms on a 12 SpecInt95 computer, (PIII 300 MHz). We nominally assume that the level 3 Hall D code will be about 10% as complicated as off-line code. We then double the requirements to account for overhead. This gives us that 0.25 SpecInt95 of processing power will allow us to analyze a level 3 event in 1 s. PIII 750 MHz processors available at the start of 2000 are rated at 35 SpecInt 95, and given the rapid advances in computer speeds, Moore's law predicts that 350 SpecInt95 processors will be available at the start of 2005, and 700 SpecInt95 processors would be available by the middle of 2006. Table 34 summarizes the needs of the Hall D level 3 system. These can easily be met by a reasonable number of processors, particularly by using dual processor nodes. We note that these numbers are small compared to FNAL experiments currently running, and very small compared to expected LHC needs. Careful and timed purchases of processors will allow us to easily accommodate the level 3 trigger. Finally, we have left open the possibility of a clever level 2 hardware trigger. If such hardware could be designed, it would reduce the requirements on the level 3 farm.

4.E.5 Data Handling

The overall strategy for handling the large volume of data produced by the Hall D detector is straightforward and similar to other large fixed-target experiments. The amount of data generated by Hall D, essentially 15 kHz, is ambitious by today's standards but should be achievable at a reasonable cost in the near future. Current technology is exemplified by the CLAS detector at

Jefferson lab, which can handle a sustained rate to tape of up to 3 kHz. The movement of data from the DAQ to the computing center for Hall D will be identical to CLAS. On-line data are staged to disk in the counting house, and moved to the computing center where it is written directly to tape. The off-line analysis will place a heavy reliance on automated tape silos to access the data for both track reconstruction and higher-level analysis.

Hall D software must be developed not only to orchestrate the movement of data but to provide an integrated reconstruction and analysis environment. A design feature of this environment must include the ability to perform the same analysis of the data in the on-line and off-line environments, to allow for extensive data-quality monitoring. This requires a common set of software tools to be used throughout the on-line and off-line software. From an organizational point of view this implies an integrated on-line and off-line software environment.

4.E.6 Partial Wave Analysis

In order to identify the J^{PC} quantum numbers of a meson, it is necessary to perform a *partial wave analysis*. In the simplest terms, a partial wave analysis is an attempt to determine production amplitudes by fitting decay angular distributions. The fit may include information on the polarization of the beam and target, the spin and parity of the resonance, the spin and parity of any daughter resonances, and any relative orbital angular momenta. The analysis seeks to establish both the production strengths and the relative phase motion between various production amplitudes. Phase motion is critical in determining if resonance production is present.

While the implementation of a partial wave analysis is, in principle, straightforward, there are both empirical and intrinsic difficulties. Empirically, instrumentation effects, such as detector acceptance and resolution, can conspire to make one distribution look like another. These similar distributions lead to leakage in the partial wave analysis. Here, cropping, smearing, or incorrect acceptance corrections of two physically different distributions may lead to distributions which are apparently indistinguishable. These difficulties can be minimized by properly designing the experiment. Full angular coverage in the distributions can be achieved by using a nearly 4π detector with excellent resolution. In addition, high statistics are critical to be able to accurately separate these partial waves. A thorough partial wave analysis requires nearly 4π coverage, excellent resolution, high statistics, and a very good understanding of the detector.

The PWA method is subject to intrinsic mathematical ambiguities for certain final states. Two or more different choices of amplitudes lead to identical observables. Here there are at least

two approaches. The first assumes some *a priori* physics knowledge that allows one to choose one solution over another. The second, and cleaner approach is to simultaneously examine several final states to which the resonance can decay. While the distributions may be confused in one final state, such as $\eta\pi$, such ambiguities are likely to be absent or different in a second such as $\rho\pi$. This latter approach assumes that the detector has been optimized for many different final states, and that relative normalizations between these are understood.

This latter approach of looking at multiple final states not only would allow one to separate different waves, but in itself yields key information about the relative decay rates of mesons. It is this latter information that is critical to understanding the underlying wavefunctions of the mesons – their content, and mixing with other states. This ability to accurately measure many final states and perform a simultaneous partial wave analysis is a key feature of the Hall D spectrometer for doing excellent spectroscopy.

The use of photon polarization will also allow one to both simplify the analysis parameterization and access additional information on the production of mesons. It will also provide key checks on the stability of the analysis itself. While circularly polarized light may yield some information in a few special cases, the true gain comes from linear polarization. Linear polarization defines a *new spatial direction* beyond the photon direction, while for circular polarization, the polarization and the momentum are in the same direction. Secondly, linearly polarized light is a coherent sum of circularly polarized light, which leads to new interference terms.

Finally, there is always a problem of background in a partial wave analysis. This limits one's ability to measure phase motion, and can be particularly severe in a region of dense overlapping resonances. Backgrounds involve a different final state accidentally reconstructing as the channel under study. Either a particle is missed by the detector, or when putting the final state back together, multiple interpretations are possible. This can be minimized with a good 4π detector with high efficiency for detecting all final-state particles with good resolution. One needs all particles to be reconstructed well enough to allow for a complete kinematic identification of a specific final state.

As part of the Hall D design studies, the group has carried out a partial wave analysis on simulated data for the reaction: $\gamma p \to \pi^+\pi^+\pi^- n$, for 8.5 GeV photons. Studies have been done with photon polarizations ranging from 0% up to 100%. The simulated data include several 3π resonances which decay via $\rho^\circ\pi^+$ to the 3π final state. The data are assumed to proceed via purely one-pion exchange. Two different packages for partial wave analysis have been used, each with a different formalism for fitting the data. The results between the two agree. The use of more than

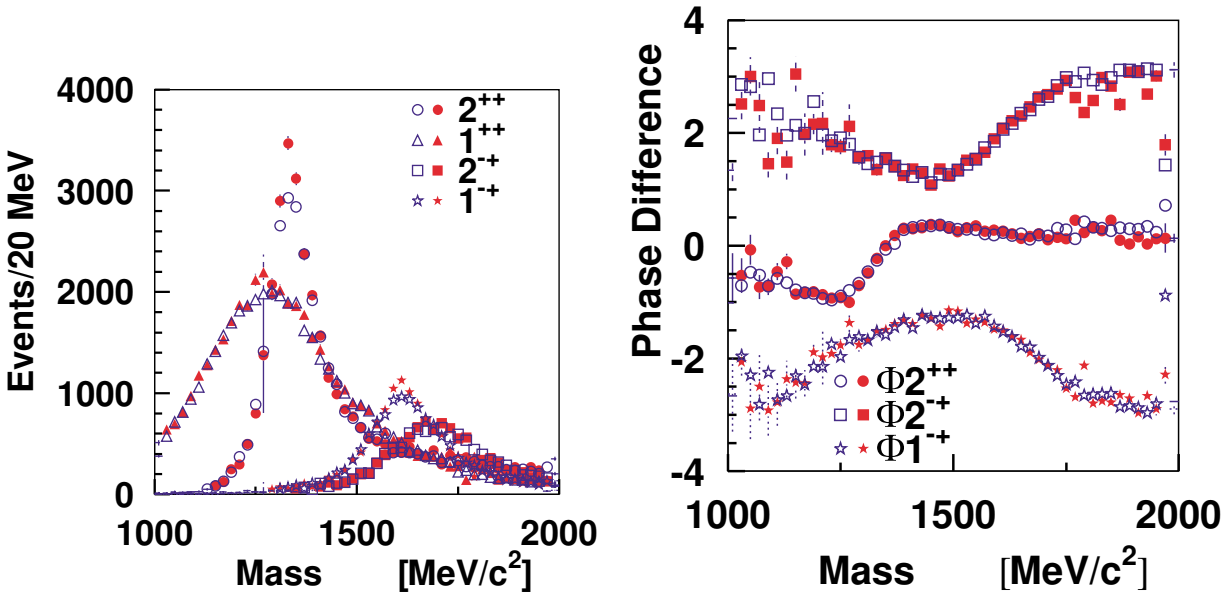

Figure 97: Partial wave analysis results for simulated 3π data. The solid figures correspond to fits to generated data, while the open figures correspond to fits to events which have been run through the Hall D Monte Carlo program. The left-hand figure shows the intensities of several waves, while the right-hand figure shows the phase difference using the 1^{++} wave as a reference.

one analysis package on real data will allow us to better access the systematics associated with the fitting of the data. The data used in these fits correspond to a couple percent of one year's reconstructed sample using 10^7 photons per second. It should be noted that this channel has a large photoproduction cross section, while the goal of the experiment is to simultaneously study channels with much smaller cross sections.

Figure 97 shows the results of fits to the simulated data. The solid figures correspond to simple generated data, while the open figures are for data which have been run through the Hall D Monte Carlo program to simulate both acceptance and resolution effects. The small differences between the two curves are due mostly to resolution, particularly for the fast π's in the events. It should be noted that the 3π channel, while one of the stronger photoproduction channels, is also one of the more difficult as far as resolution goes. The curves correspond to the $a_2(1320)$, ($J^{PC} = 2^{++}$), the $a_1(1260)$, (1^{++}), the $\pi_2(1670)$, (2^{-+}), and an exotic $\pi_1(1600)$, (1^{-+}). The phase differences are plotted with respect to the $a_1(1260)$ wave.

In addition, two small partial waves that together represent less than 1% of the total intensity have also been fit. In this model, these waves correspond to a second decay modes for the $a_1(1260)$

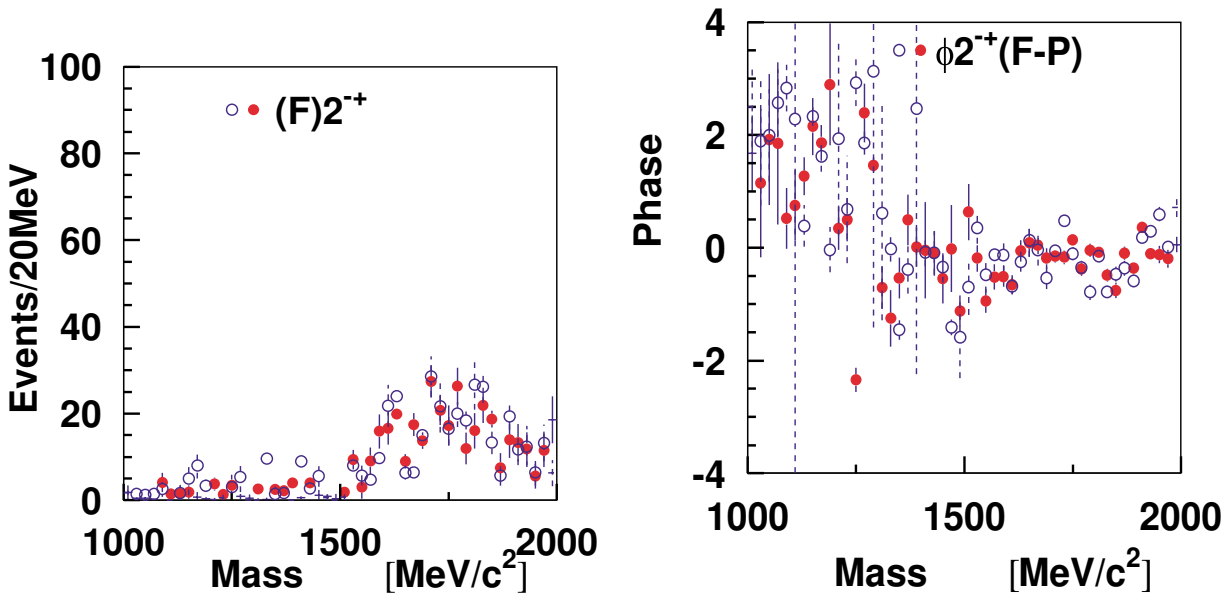

Figure 98: Partial wave analysis results for simulated 3π data. The solid figures correspond to fits to generated data, while the open figures correspond to fits to events which have been run through the Hall D Monte Carlo program. These figure correspond to the F-wave decay of the $\pi_2(1670)$, which is less than 1% of the entire signal. The two important features are the small signals in the intensity and the phase difference plot. The phase difference is relative to the dominant decay of the π_2 and should be zero (as it is).

in which the $\rho\pi$ have two units of angular momentum between them, and for the $\pi_2(1670)$ in which the $\rho\pi$ have three units of angular momentum between them. The ratios of these second modes to the main mode are important quantities in their own right. The main issue here is that the partial wave analysis has been able to extract these signals from the data. Figure 98 shows the intensity and phase difference for the $\pi_2(1670)$. The phase difference is measured with respect to the dominant $L = 1$ decay of the π_2 and should be near zero. This is clearly the case where there is strength in the intensity plot.

Similarly, a study on the effect of linear polarization in determining the production mechanism has been undertaken. In the Gottfried-Jackson frame of the decaying resonance, the angle α is defined to be the angle between the polarization vector of the photon and the normal to the production plane of the reaction. In the case of unpolarized photons, this angle is not defined. When α is either 0° or 90°, the photon is in a well-defined state of reflectivity. In the case of single pion exchange (the naturality of the π is negative), the produced reflectivity state of the resonance is opposite to that of the photon. In the case of natural parity exchange (such as ρ exchange), the

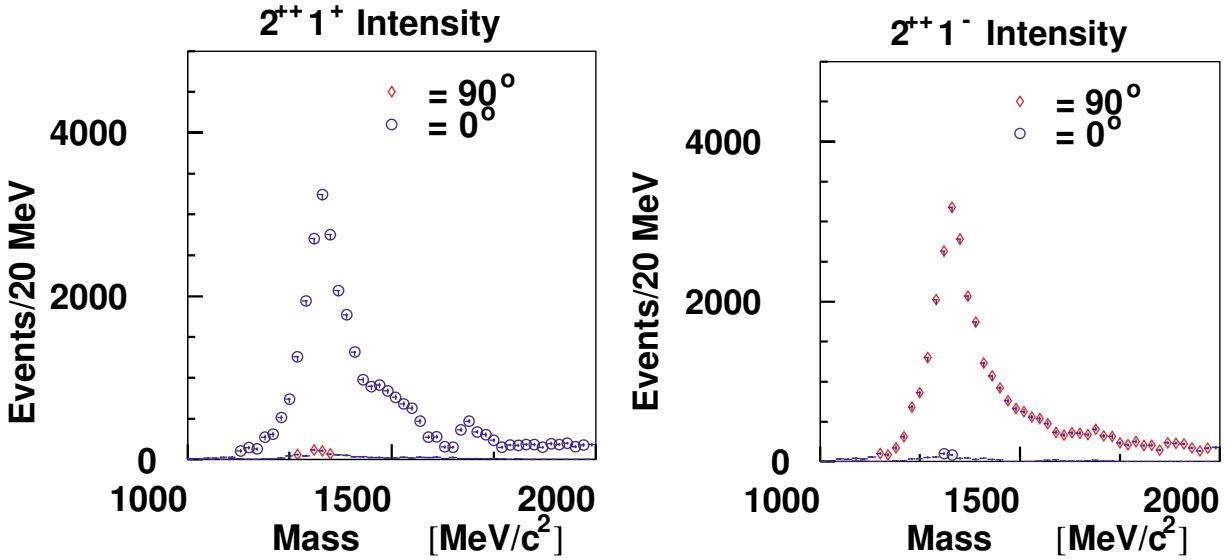

Figure 99: Left: The fit to the positive reflectivity part of the 2^{++} intensity for events near $\alpha = 0°$ and 90°. Right: The same for the negative reflectivity waves. They key point is that the positive reflectivity wave is produced near $\alpha = 0°$ while the negative reflectivity is produced near $\alpha = 90°$. See the text for a more complete discussion.

two reflectivities will be the same. A pair of partial wave analyses has been done in which we have selected only events near $\alpha = 0°$ or $\alpha = 90°$. Figure 99 shows the results for the 2^{++} wave. The figure on the left shows the positive reflectivity 2^{++} wave, $\mid M \mid^{\epsilon} = 1^{+}$. Only the events near $\alpha = 0°$ contribute, while the $\alpha = 90°$ gives nearly no contribution. The exact opposite happens in the $\mid M \mid^{\epsilon} = 1^{-}$ wave on the right. Had the production mechanism been of opposite naturality to the pion, these figures would have been reversed. If both mechanisms had been present, then the exact mixture could have been read directly off these plots. Of course the real data will involve a more general fit to this in which the degree of linear polarization is used. However, linear polarization allows the naturality of the exchange particle to be trivially known, while for no linear polarization, there is no such handle on this.

4.E.7 Hall D Summary

The Hall D beam and detector have been optimized to perform a good partial wave analysis of mesons and baryons produced with an 8 to 9 GeV linearly polarized photon beam. Even with rates of only $10^7\,\gamma/s$, the experiment will collect at least an order of magnitude more data than existing π beam experiments during its first year of running. Such an increase in statistics coupled with

a new production mechanism will not only allow us to map out the gluonic excitations, but to measure their decay properties and production mechanisms as well.